MAVEN/NGIMS Dayside Exospheric Temperatures over Solar Cycle and Seasons: Role of Dayside Thermal Balances in Regulating Temperatures

S. W. Bougher[1], M. Benna[2], M. Elrod[2], K. Roeten[1], E. Thiemann[3]

[1]CLaSP Department, University of Michigan, Ann Arbor, MI 48109 USA

[2]NASA Goddard Space Flight Center, Greenbelt, 20771 MD USA

[3]LASP, University of Colorado, Boulder, CO 80309 USA

Key Points:

- MAVEN dayside temperatures are shown to vary by 80 K ($\sim$180-260 K) over solar cycle 24, reduced from the MGS value of 120 K.
- Mars temperature versus EUV sensitivity is similar for MAVEN and MGS exospheric measurements at 38 and 45 K m^2 mW^{-1}.
- Mars thermal conduction balances EUV heating (160-180 km) for solar maximum conditions, while CO_2 cooling is secondary.

Corresponding author: S. W. Bougher, bougher@umich.edu

Abstract

Several important processes of the Mars upper atmosphere are regulated by exospheric temperature (Texo) variations, including atmospheric escape rates. From the MAVEN mission, significant and largely periodic variability of Mars dayside Texo is now revealed by Neutral Gas and Ion Mass Spectrometer (NGIMS) datasets collected throughout solar cycle 24. Two complementary methods are utilized to extract temperatures from NGIMS datasets. These NGIMS dayside mean exospheric temperatures are shown to vary by $\sim$80 K ($\sim$180-260 K) over solar cycle 24. This corresponds to a ΔTexo/ΔEUV sensitivity of $\sim$38 K m^2 mW^{-1}, where Lyman-α is the solar index. Previous Mars Global Surveyor (MGS) derived Texo values for solar cycle 23 yielded a sensitivity of $\sim$45 in the same units. This close correspondence suggests that the underlying dayside energy balances are similar yet slightly different over these two solar cycles. Corresponding Mars Global Ionosphere-Thermosphere Model (M-GITM) simulations show that molecular thermal conduction largely balances EUV heating for the Mars dayside thermosphere, while CO_2 15-μm cooling is secondary in importance, along with global winds. It is valuable to compare this Mars sensitivity to that computed for the dayside thermosphere of Venus. Pioneer Venus dayside datasets imply a sensitivity of $\sim$17.5 K m^2 mW^{-1} units for solar cycle 21, a factor of $\sim$2.2 smaller than computed for Mars. This is because Venus CO_2 cooling strongly balances EUV heating near its peak, thereby serving as a more efficient thermostat regulating dayside temperatures. CO_2 cooling is much weaker for Mars.

Plain Language Summary

Modern Earth global warming of its lower atmosphere is complemented by enhanced CO_2 15-μm cooling in its upper atmosphere. This CO_2 cooling process also has a role in the CO_2 dominated upper atmospheres of Venus and Mars. From the MAVEN mission, significant and largely periodic variability of Mars dayside exospheric temperatures is revealed by Neutral Gas and Ion Mass Spectrometer (NGIMS) datasets collected during the declining phase of the solar cycle (2014-2019). These NGIMS dayside mean exospheric temperatures vary by $\sim$80 K (180-260 K) over this weak (low sunspot number) solar cycle 24. Corresponding Global Climate Model (GCM) simulations of the Mars upper atmosphere reproduce this 80 K variability, revealing Extreme Ultraviolet heating is largely conducted downward to lower thermosphere altitudes providing net cooling, while CO_2 15-μm cooling is secondary in importance. By contrast, Pioneer Venus Or-

–2–

biter dayside datasets (1978-1992) also imply a similar ∼80 K variability at Venus, now for the very strong (∼3-times larger sunspot number) solar cycle 21. GCM simulations for Venus determine that CO_2 cooling strongly balances EUV heating near its peak, thereby serving as an efficient thermostat regulating dayside temperatures. CO_2 cooling is much weaker for Mars, yielding larger solar cycle variations in exospheric temperatures.

1 Introduction and Background

The Mars dayside thermal structure of its upper atmosphere can change dramatically over time since its energy balance is typically controlled by two highly variable components of the Sun's energy output: solar radiation (∼0.1–200 nm) and solar wind particle precipitation (e.g. Bougher et al., 2002, 2009; Bougher, Brain, et al., 2017; Fang et al., 2013). Usually, soft X-ray (0.1–5 nm) and EUV (5–110 nm) solar radiation is responsible for heating the Mars thermosphere and forming its ionosphere. These contributions vary significantly over time. Specifically, both solar rotation (∼27-day periodic) and solar cycle (∼11-year periodic) variations of these solar fluxes are significant, producing dramatic variations in global thermospheric temperatures, composition, and resulting winds (e.g. Bougher et al., 2000, 2002, 2009; Forbes et al., 2008), as well as ionospheric densities (e.g. Fox, 2004). Furthermore, this solar radiation received at Mars varies by ± 22% throughout the martian year, solely the result of the periodic change of the heliocentric distance. Conversely, solar wind particle fluxes and resulting energy deposition into the Mars thermosphere are largely episodic in nature (e.g. Fang et al., 2013).

This study is motivated by the significant and largely periodic variability of Mars dayside exospheric temperatures (Texo) revealed by new MAVEN Neutral Gas and Ion Mass Spectrometer (NGIMS) datasets (e.g. Benna et al., 2015; Bougher, Roeten, et al., 2017; Stone et al., 2018). Several important features of the Mars upper atmosphere are driven by Texo variations. For instance, exobase temperatures are a key state variable that impacts atmospheric escape (e.g. directly via Jeans escape, indirectly via hot O/H escape). For example, extremes of the solar cycle and seasonal variability indeed impact hot oxygen escape rates (e.g. Lee et al., 2015). Furthermore, it is important to constrain the relative role of O enhanced CO_2 15-μm cooling at Mars in the context of its unique role at Venus, Earth and Mars (e.g. Bougher et al., 1999). The same O-CO_2 deactivation rate coefficient should apply to all three terrestrial planets. This three planet comparison is made possible by leveraging new detailed O abundances now constraining Mars

–3–

CO$_2$ cooling, and its role in regulating dayside temperatures (Mahaffy et al., 2015; Bougher et al., 2015b). Finally, characterization of modern Mars dayside thermosphere temperatures (and associated heat budgets) is a crucial step for properly benchmarking subsequent ancient Mars calculations of thermosphere-ionosphere structure and volatile escape.

1.1 pre-MAVEN datasets of dayside exospheric temperatures

The combined solar cycle and seasonal variations in martian dayside thermosphere (and exosphere) temperatures have been the focus of considerable investigation and analysis since the early Mariner Ultraviolet Spectrometer (UVS) measurements (1969–1972), and proceeding to recent Mars Atmospheric and Volatile Evolution Mission (MAVEN) measurements (2014–present) (see also section 2.1) (e.g. A. I. F. Stewart, 1987; Bougher et al., 1999, 2000, 2009; Bougher, Brain, et al., 2017; Keating et al., 2003, 2008; Withers, 2006; Leblanc et al., 2006; Forbes et al., 2008; González-Galindo et al., 2009; Krasnopolsky, 2010; Huestis et al., 2010). Even before MAVEN, it was clear that the significant Mars eccentricity demands that both the solar cycle and seasonal variations in near exobase temperatures be considered together in the characterization of their solar driven (periodic) values (e.g. Bougher et al., 2000, 2015; Bougher, Brain, et al., 2017). For example, 3-D model simulations previously compared Equinox simulations with both Aphelion and Perihelion seasonal Texo values (for the same intrinsic solar minimum and maximum EUV fluxes, respectively) and found dayside Texo differences of $\Delta T \sim 25\text{-}40$ K (Bougher et al., 2015). By contrast, predicted solar cycle variations (for constant Equinox season) are much larger ($\Delta T \sim 120\text{-}130$ K).

Near solar minimum, dayside low solar zenith angle (SZA) Texo values have previously been extracted from the Viking 1 entry science data sets ($\sim$186 K) (e.g. Nier & McElroy, 1977; Seiff & Kirk, 1977), MGS accelerometer density scale heights ($\sim$190–200 K) (Withers, 2006; Keating et al., 2008), and from Mars Express SPICAM UVS airglow scale heights ($\sim$201$\pm$ 10 K) (Leblanc et al., 2006). These limited spacecraft measurements were used before MAVEN to characterize Mars Texo for near solar minimum, aphelion conditions. Conversely, solar moderate-to-maximum, near perihelion Texo values were estimated from Mariner 6-7 CO Cameron emissions ($\sim$315 K) (e.g. A. I. Stewart, 1972), and Mariner 9 CO Cameron emissions ($\sim$325 K) (A. I. Stewart et al., 1972). Perhaps the most comprehensive pre-MAVEN study of Texo utilized MGS drag measurements

–4–

111 (from the precise orbit determination method) near ~390 km (Forbes et al., 2008; Bougher

112 et al., 2009) to reveal dayside Texo spanning ~170-180 to ~300 K, appropriate for so-

113 lar cycle # 23 (SC23) conditions. Overall, a composite estimate of the "extreme" solar

114 cycle plus seasonal variation of Mars dayside exospheric temperatures of about ~100–

115 140 K was estimated before MAVEN (Bougher, Brain, et al., 2017). These estimates are

116 all based on measurements obtained during solar cycles # 19-23.

1.2 Early-MAVEN datasets of dayside exospheric temperatures

118 Early-MAVEN mission characterization of dayside solar cycle exospheric temper-

119 ature variations for Mars was addressed by initial NGIMS, IUVS and EUVM (Extreme

120 Ultraviolet Monitor) instrument studies for which only a portion of solar cycle #24 mea-

121 surements were available (Bougher, Roeten, et al., 2017; Jain et al., 2015; E. M. Thie-

122 mann et al., 2018). In these studies, extracted Texo values for near overlapping sampling

123 periods yielded reasonable comparisons of IUVS and NGIMS temperatures. EUVM so-

124 lar occultation studies revealed CO_2 densities and exospheric temperatures at dawn and

125 dusk locations for perihelion and aphelion seasons. Overall, solar cycle trends were found

126 to be consistent with pre-MAVEN measurements (see section 1.1). Later, Stone et al.

127 (2018) carried out a careful analysis of NGIMS extracted temperatures (vertical profiles)

128 from 8-Deep Dip campaigns. Both solar cycle and diurnal variations of thermospheric

129 temperatures (including Texo) were derived. In addition, initial heat balance terms for

130 reproducing Deep Dip #2 temperatures were derived from a 1-D model, necessarily fo-

131 cused on radiative terms and neglecting global dynamics. The need for a full 3-D model

132 treatment (including large scale winds) is important to address the dynamical processes

133 contributing to the maintenance of NGIMS temperature profiles.

134 Most recently, a comprehensive investigation making use of nearly 4-Martian years

135 of IUVS dayside airglow derived thermosphere and mesopause temperatures was con-

136 ducted (Jain et al., 2021). This study covers solar cycle #24 (SC24) measurements from

137 MAVEN. A few important findings are as follows: (a) thermospheric temperatures show

138 strong long-term variability, for which temperatures are largely driven by solar EUV vari-

139 ations and Mars seasons; (b) the thermosphere tends to be colder in the morning hours

140 compared to the evenings where the temperatures are higher; (c) temperatures from both

141 the Martian thermosphere and mesosphere show strong short-term variability indicat-

142 ing coupling from the lower atmosphere, and (d) this seasonal and solar cycle dependence

of dayside thermospheric temperatures was largely predicted by global models (e.g. González-Galindo et al., 2015; Bougher et al., 2015) prior to MAVEN.

1.3 New approach using 6-years of NGIMS exospheric temperatures

In this paper, we examine the solar cycle variation of the dayside Texo over the MAVEN mission throughout solar cycle #24 - (SC24). The dataset of MAVEN NGIMS scale height temperatures spans dayside local times at all latitudes and seasons (for SZA $\leq$ 60 degree). This enables a statistical picture of dayside Texo solar cycle variations to be made first, followed by key seasonal and SZA dependencies next. This NGIMS study is complementary to that conducted from the IUVS instrument described in section 1.2 (Jain et al. 2021).

For consistency, we validate the Texo derivation from the scale height technique using 8-specific NGIMS sampling periods (SZA $\leq$ 60 degree) now applying a hydrostatic integration technique. This validation is meant to confirm the robustness of the scale height derived exospheric temperatures for our studies.

These newly derived MAVEN Texo variations are placed into context by comparing to pre-MAVEN Texo variations from Mars Global Surveyor (MGS). Comparison between MGS and MAVEN Texo datasets is achieved using a common sensitivity calculation for which Lyman-α is selected as a proxy of solar EUV fluxes providing heating to the upper atmosphere.

A brief outline of the sections of this paper is as follows. Section 2 provides descriptions of the MAVEN datasets used in this study. Section 3 provides an overview of the M-GITM modeling framework and its usage to compute Texo variations over solar cycle #24 and the corresponding thermal balances that drive these variations. Section 4 presents NGIMS data analysis Texo trends as well as M-GITM modeling outputs that serve to interpret these NGIMS observations. Section 5 provides a comparative planetology view by comparing Mars and Venus Texo variations and underlying thermal balances. Finally, section 6 finishes with a summary and conclusions.

2 MAVEN Datasets Used in this Study

NGIMS is a quadrupole mass spectrometer on the MAVEN spacecraft designed to measure the densities of major neutral and ion species in the upper atmosphere with a

vertical resolution of <5 km and an accuracy of <25% for most species. Measurements are made at altitudes between 150 and 500 km along the inbound and outbound segments of the elliptical science orbit (SO). Excursions to altitudes as low as ∼125 km were completed during 9 week-long "Deep Dip" (DD) campaigns. NGIMS leverages its dual ionization sources to measure both key non-reactive neutral species (e.g. CO_2, Ar, N_2, He), and surface reactive neutral species (e.g. O, CO) and as well as ambient ions (e.g. Mahaffy et al., 2015; Benna et al., 2015; Benna & Elrod, 2020).

Our studies utilize NGIMS Level 2, Version 8, Revision 1 (V08_R01) neutral and ion densities and Level 3 Version 6, Revision 1 (V06_R01) scale height extracted temperature products spanning MAVEN periapsis to exobase altitudes. This most recent density data includes corrections for CO densities following extensive recalibration studies (Benna & Elrod, 2020). See details in sections 2.2.1 and 2.2.2 below.

Lastly, solar fluxes measured at Mars are provided from the Extreme Ultraviolet Monitor (EUVM) instrument. See section 2.1 below.

2.1 EUVM solar fluxes used for data analysis and M-GTIM simulations

MAVEN Extreme Ultraviolet Monitor (EUVM) daily fluxes from the FISM-M empirical model (an L3 product, V14_R3) (E. M. B. Thiemann et al., 2017) are used to supply inputs to the M-GITM numerical model for calculating solar EUV-UV heating, photo-dissociation, and photo-ionization rates (see section 3.1). These FISM-M fluxes correspond to the NGIMS orbits following a daily cadence with sub-daily values interpolated for the specific orbit. The FISM-M spectral intervals (∼0.1 to 210 nm) are rebinned for the 59-wavelength intervals (and associated cross sections) captured by the M-GITM model (0.1 to 175.0-nm) (Bougher et al., 2015). In addition, the Lyman-α index used in this paper (i.e. proxy for EUV fluxes as a whole) is taken from this same empirical model. In this regard, these Lyman-α fluxes will be used to derive a correlation with NGIMS derived exospheric temperatures for the generation of a least-squares empirical trend (see Figure 1). The slope of this linear trend is designated the ΔTexo/ΔEUV sensitivity, a key parameter for discussion in this paper. See section 4.1 for a detailed discussion.

Lyman-α fluxes are chosen as the proxy for EUV fluxes in this paper for three reasons: (a) this index has been well measured from Earth for many years, and is tabulated in the LISIRD electronic database at LASP (Machol et al., 2019), (b) this Earth based

–7–

index can easily be shifted to the Mars-Sun line orientation for interpolation to Mars, and (c) the available Pioneer Venus proxy for EUV solar fluxes is best tied to measured Langmuir Probe (LP) current, which is dominated by Lyman-α fluxes (see section 5). The ultimate goal in choosing this common index is to compare the ΔTexo/ΔEUV sensitivities for Venus and Mars, both CO_2 dominated planets.

2.2 MAVEN NGIMS datasets of densities and derived temperatures

2.2.1 Details of L3 datasets: Overview Texo sampling method

The L3 scale height and temperatures are high level products derived from the L2 abundances. The L3 data typically span the altitude range of the CO_2 exobase to the periapsis. This valuable dataset provides topside (near traditional exobase) scale heights for key species as measured by the NGIMS instrument. These scale heights are determined by linear fits of altitude versus log (density) between the periapsis and the exobase altitude (Benna & Elrod, 2020). The exobase altitude is defined by computing the altitude where the overhead integrated density accounts for one mean free path for CO_2 molecules. This method works for each orbit for which periapsis altitudes $\leq$185 km (prior to MAVEN periapsis raise in mid-June-2020). This condition is relevant to all SC24 NGIMS orbits used in this paper. Retrieval of scale height temperatures for periapsis altitudes above 185 km will be outlined in a future publication, and is beyond the scope of this paper.

For this study, we utilize Argon densities and derived scale heights and temperatures. Being a non-reactive species with a low sticking coefficient, Argon does not interact with the sensor's internal surfaces. Therefore, its measured altitude profile is immune to background variations observed for reactive species due to gas/surface buffering (Mahaffy et al., 2015). This scale height derivation method can be applied rapidly across $\sim$12000 NGIMS orbits for computing exospheric temperatures (Texo) and their variations over solar cycle, season and SZA (see Figures 1 and 2).

The uncertainties for NGIMS scale height derived exospheric temperatures were computed for each orbit. The error method is stated in the NGIMS PDS Software Interface Specification (Benna and Elrod, 2020). Basically, using a linear regression method produces a correlation and error. The temperature errors (Temp-error) reported in the L3 dataset are the residuals from the least squares fit for each orbit sampled. Specifi-

cally, we performed a chi-square fit of the trend with uncertainty determination. Typical temperature errors are about ±50 K (see Table 1 caption). In summary, all temperature uncertainties (Temp-error) from the linear fit of each orbit are included within the L3 files. These Temp-error values are now incorporated into the solar cycle linear fits presented (or used) in Figures 1, 2, and 3.

2.2.2 *Details of L2 datasets: Overview Texo sampling method and Specific Intervals*

Temperatures can also be extracted from the NGIMS L2 datasets by vertically integrating CO_2 or Argon densities from the top down to obtain pressures (Bougher, Roeten, et al., 2017). The L2 data along the in-situ aeropass can have a ∼0.9-1.0 km vertical resolution near 200 km, and very small vertical resolution near the periapsis (where the spacecraft horizontal motion is significant). For the present work, the vertical density profile is assumed to be in hydrostatic equilibrium, and the hydrostatic equation is integrated for Ar densities to obtain the local partial pressure. From additional application of the ideal gas law, temperatures can be computed. This same basic method of deriving temperature profiles from densities was recently used in Bougher, Roeten, et al. (2017) and Snowden et al. (2013). For the hydrostatic integration, a range of pressures for the upper boundary condition have been tested (i.e. Bougher, Roeten, et al., 2017) to determine their impacts on the resulting topside temperature profile. It was found that the temperature profile was negligibly altered by the choice of upper boundary condition below a certain altitude range, which was typically ∼220 km for near perihelion conditions and ∼200 km for near aphelion conditions. Additionally, for the lower altitudes of the profile, it should be noted that near periapsis, in particular, there is a more significant horizontal component to the spacecraft trajectory, and thus variations along the measured density profile (Stone et al., 2018). In order to better ensure the hydrostatic integration is appropriate, the temperature profiles examined here are limited to altitudes approximately a scale height above the orbit periapsis. Correspondingly, the altitude region of near isothermal temperatures used for this analysis was ∼200-220 km for perihelion/solar high conditions and ∼180-200 km for aphelion/solar low conditions. These two altitude ranges for these different periods approximately correspond to the CO_2 density interval of ∼10^8 to 10^7 cm^{-3}. Therefore, we elect to extract Texo values making use of this CO_2 density interval criteria.

Table 1 outlines 8-intervals (key selected campaigns) for extraction of NGIMS 1-D temperature profiles and associated exospheric temperatures. Only SZA = 0-60° conditions are sampled, spanning solar minimum/aphelion to solar maximum/perihelion conditions encountered during the MAVEN mission (during SC24). The altitude range for the derivation of Texo values is 180-200 km for solar low conditions, while 200-220 km is used for solar high conditions. For this paper, solar high and low values are defined as periods above and below the Lyman-alpha flux of $\sim$3.5 mW/m^2, respectively. Period # 1 (DD2 extended) covers $\sim$140 orbits (nearly 28 days), in order to smooth out variations of exospheric temperatures due to solar rotation (Bougher, Roeten, et al., 2017; Jain et al., 2015). Most subsequent periods contain $\sim$60-70 orbits (nearly 5-full longitude sampling cycles over 13-15 days); solar rotation variations are expected to be small after mid-October 2016 during the declining phase of solar cycle #24. Periods #6 and 7 span the full duration of DD8 and DD9 campaigns only, about 6-7 days each. Lastly, these computed 8-period mean exospheric temperature values are compared to the computed ΔTexo/ΔEUV sensitivity and linear trends extracted from scale height temperatures derived from MAVEN NGIMS dayside observations (see Figure 3, Table 1). The detailed justification for this linear trending, and associated error analysis, are provided in section 4.1.

The method of extracting temperatures through vertical integration of the hydrostatic equation allows the derivation of entire profiles. However, this technique is laborious and time consuming when applied to thousands of NGIMS orbits. Instead, its application to a limited number of orbits (e.g. Deep Dip campaigns) for detailed vertical structure studies is preferred (e.g. Stone et al., 2018). An independent method for calculation of exospheric temperatures is given in section 2.2.1, based upon local scale heights in the near isothermal region above about $\sim$180 km. This simpler method allows much faster processing of the large number of NGIMS orbits. We have used such scale height derived Texo values in Figures 1 and 2.

2.2.3 Specific campaigns of L2 datasets: Detailed studies of extremes

Two specific intervals are chosen for detailed study of the extremes of the exospheric temperatures owing to the combination of solar cycle and seasonal variations. The two campaigns chosen are: (a) the Deep Dip 2 extended campaign (orbits 1059-1200) for low SZA and early MAVEN solar maximum conditions approaching vernal equinox (Ls $\sim$

–10–

Table 1. Specific MAVEN 8-periods (campaigns) for extracting 1-D NGIMS temperature profiles and associated exospheric temperatures from the hydrostatic integration method (L2-Texo). Only SZA = 0-60 degree is sampled, from which ΔTexo/ΔEUV sensitivity is extracted and compared to pre-MAVEN and MAVEN values (see Table 3). L3-Texo corresponds to scale height derived Texo. The 1-σ tabulated values correspond to the standard deviation of the orbital dispersion about the period mean Texo. DD2E corresponds to an extended Deep Dip 2 campaign interval. DD8 and DD9 correspond to MAVEN Deep Dip 8 and 9 campaigns, respectively. PC19 corresponds to the post-conjunction period in 2019. The number of days for data processing in each period is tabulated. Typical temperature uncertainties gleaned from the L3-Texo method are about ±50 K. L2-Texo derived temperature errors are related to Argon density uncertainties themselves and atmospheric wave structure (e.g. Stone et al., 2018) and are on the same order as L3 errors (±30-50 K). Text describes comparison of the two methods.

Period	Dates	Ls and Orbit (range)	SZA (range)	# Days (MY)	L2-Texo(K) (1-sigma)	L3-Texo(K) (1-sigma)
1 (DD2E)	15-Apr-15 to 13-May-15	328-341 (1059-1200)	6-42	28 (32)	252±43.3	246.7±31.3
2	15-Oct-16 to 27-Oct-16	250-270 (3982-4045)	49-59	13 (33)	224.5±22.0	226.9±15.4
3	9-Apr-17 to 23-Apr-17	340-360 (4900-4971)	40-54	15 (33)	233.8±36.8	239.9±20.1
4	4-May-17 to 16-May-17	0.0 (5029-5095)	32-34	13 (33)	209.2±50.3	202.8±21.2
5	20-Sept-17 to 2-Oct-17	60-80 (5769-5836)	45-59	13 (34)	190.1±27.7	196.2±18.4
6 (DD8)	16-Oct-17 to 22-Oct-17	75-77 (5909-5946)	20	7 (34)	187.3±40.6	188.6±27.9
7 (DD9)	23-Apr-18 to 28-Apr-18	160-180 (6931-6961)	54-60	6 (34)	211.1±39.8	205.9±15.5
8 (PC19)	16-Sept-19 to 30-Sept-19	84-86 (9929-10017)	38-40	15 (35)	185.8±40.9	185.7±40.0

299 328-341), and (b) the post-solar conjunction 2019 (orbits 9926-10017) for low SZA and

300 late MAVEN solar minimum conditions near aphelion (Ls $\sim$ 85.0). These cases are cho-

301 sen to investigate the M-GITM performance during Mars seasonal/solar cycle extreme

302 conditions, and to be consistent with deep dayside sampling (SZA $\leq$ 60 degrees) for com-

303 parison to NGIMS statistical exospheric temperature trends illustrated in Figures 1 and

304 3.

3 Three-dimensional Modeling of Texo Variations using M-GITM

306 The Mars Global Ionosphere-Thermosphere Model (M-GITM) is a 3-D spherical

307 code that was developed to address the physics of the whole Mars atmosphere system,

308 capturing the basic observed features of the dynamical, thermal, and composition of the

309 atmosphere from the surface to $\sim$250 km (Bougher et al., 2015). The M-GITM code was

310 built from the terrestrial GITM framework (Ridley et al., 2006), now including Mars fun-

311 damental physical parameters, ion-neutral chemistry, key radiative processes, and solar

312 (insolation/particle) and dynamical (wave/tidal) drivers unique to Mars (Bougher et al.,

313 2015). Typically, the M-GITM non-hydrostatic model is setup to run with a 5°x 5° latitude-

314 longitude grid, and a 2.5 km vertical resolution. Thusfar, it has been used to interpret

315 Mars upper atmosphere features observed from several MAVEN instruments (i.e. NGIMS,

316 IUVS and ACC measurements). This includes thermospheric temperatures and key den-

317 sities throughout Mars seasons and SC24, lighter species density distributions (i.e. he-

318 lium), mass density distributions during Deep Dip campaigns, thermospheric winds dur-

319 ing short campaigns, and 2018 global dust storm impacts on the upper atmosphere (e.g.

320 Bougher et al., 2015b; Bougher, Roeten, et al., 2017; Zurek et al., 2017; Roeten et al.,

321 2019; Jain et al., 2020; Elrod et al., 2017, 2020; Gupta et al., 2021).

322 This ground to exosphere numerical model is constructed using existing parame-

323 terizations and physical formulations found in other modern GCMs (see details in Bougher

324 et al. (2015)). For instance, a correlated-k radiative transfer code is used to compute LTE

325 CO_2 15-micron cooling and near IR heating rates, both employed in the calculation of

326 lower atmosphere temperatures (0-80 km) (Haberle et al., 1999). For the Mars upper at-

327 mosphere ($\sim$80 to 250 km), a fast and modern formulation for non-LTE CO_2 15-micron

328 cooling is now used within the M-GITM code from González-Galindo et al. (2013) to ac-

329 curately capture the CO_2 cooling rates (Bougher, Roeten, et al., 2017), especially near

330 the mesopause and on the nightside.

–12–

In order to better understand Mars' lower and upper atmosphere coupling, an existing gravity wave momentum and energy deposition code (e.g. Yiğit et al., 2008; Medvedev et al., 2015) has been incorporated, implemented, and fully tested within the M-GITM framework (Roeten et al., 2022). It is a spectral non-linear scheme for the treatment of non-orographic gravity waves that reach the thermosphere from their launching point at the top of the planetary boundary layer. This scheme is one of the most recent parameterizations appropriate for gravity waves that propagate to thermospheric altitudes. It accounts for wave dissipation due to molecular viscosity in the upper atmosphere, molecular thermal conduction, radiative damping, and breaking-saturation (Roeten et al., 2022). This gravity wave scheme is now utilized when conducting new M-GITM simulations described in this paper. Standard gravity model parameters utilized in M-GITM are discussed in detail in Roeten et a. (2022). The most important thermospheric impacts resulting from application of this new GW scheme are twofold: (a) the reduction of global winds by nearly a factor of two for all Mars seasons, and (b) the cooling of temperatures above ~100 km at all latitudes, with most pronounced cooling at high/polar latitudes. It is important to emphasize that modern M-GITM simulations utilizing this new gravity wave formulation are able to capture these stated mean impacts on winds and temperatures, but not the individual impacts of gravity waves launched upward and breaking at thermospheric heights. Thus, M-GITM cannot capture any large stochastic variability that may be present in the NGIMS temperatures.

Inputs for two extreme cases are prescribed for new M-GITM simulations in this paper (see section 2.2.3): (a) a solar maximum near perihelion case capturing Deep Dip 2 conditions (and beyond) early in the MAVEN mission (2015), and (b) a solar minimum aphelion case appropriate to post-solar conjunction conditions in late 2019. These cases are specifically chosen to capture afternoon conditions (SZA $\leq$ 60 degrees) for comparison to the extremes of the NGIMS statistical Texo trend illustrated in Figure 3. In addition, the same dust scenario was purposefully chosen for all M-GITM simulations (globally uniform $\tau = 0.5$ optical opacity for averaged non dust storm conditions throughout the Mars year). This avoids the issue of the changing impact of dusty events on Texo values, that is still a focus of intense research (e.g. Fang et al. 2021 and Jain et al 2020). Finally, the maximum eddy diffusion coefficient was set to be slightly larger (1.3 factor enhancement) for solar minimum conditions, in line with weakened solar control of the thermosphere and stronger wave variability overall (Jain et al., 2021).

4 Results

4.1 Analysis of NGIMS derived Texo

First, this section provides a broad statistical picture of Texo variations over SC24. Then it shows both seasonal and SZA dependencies. Ultimately, an empirical expression for the NGIMS ΔTexo/ΔEUV sensitivity is computed. This sensitivity will be used to detrend the entire Texo dataset, revealing SZA and Ls (seasonal) dependencies. Finally, a comparison of both MAVEN and MGS trends and sensitivities is made.

The question of using a linear (least-squares) fit to capture the Mars solar cycle/seasonal trend of dayside Texo is important to address because the NGIMS scale height temperature data has a rather large scatter as shown in Figure 1. The adequacy and uniqueness of a computed linear fit for such a large scatter would be legitimate for a data distribution that is both homogenous and representative (enough data points to capture the full distribution). Thus, a robust NGIMS linear fit must meet two criteria. First, the data must follow the same distribution along the independent variable domain (EUV radiation in Figure 1 and SZA in Figure 2). If the data distribution looks the same for any sub-sample along the X direction then the data has a homogenous distribution. In that case, one can apply the classical statistical metrics such as mean, variance, etc. Secondly, if an adequate sample size is available for the distribution (i.e. if the sample is large enough), then the statistical metrics are unique. In this regard, the NGIMS scale height temperatures were analyzed and found to be statistically homogeneous along the EUV and SZA scales (see Supplement Figure S1). In both cases, the data obeys a normal-like distribution with varying mean but constant variance. Statistical homogeneity and the large size of the data set allows us to apply a linear regression and moving averaging in our analysis.

Figure 1 shows NGIMS scale height derived exospheric temperatures (Texo) as a function of the Lyman-α index (measured at Mars) over most of the MAVEN mission (i.e. solar cycle # 24). Sampling is restricted to SZA = 0-60° and LT = 6-18 and spans $\sim$12000 orbits. Ls (season) is color coded as indicated by the color bar. A linear regression (least squares) empirical trend in these Texo values is computed and superimposed (black line) spanning the 2.0-4.5 mW/m^2 solar fluxes. The dashed curves represent the uncertainty of the NGIMS linear fit due to the errors in the scale height Texo values themselves. These errors are larger for solar high conditions. It is noteworthy that a large vari-

–14–
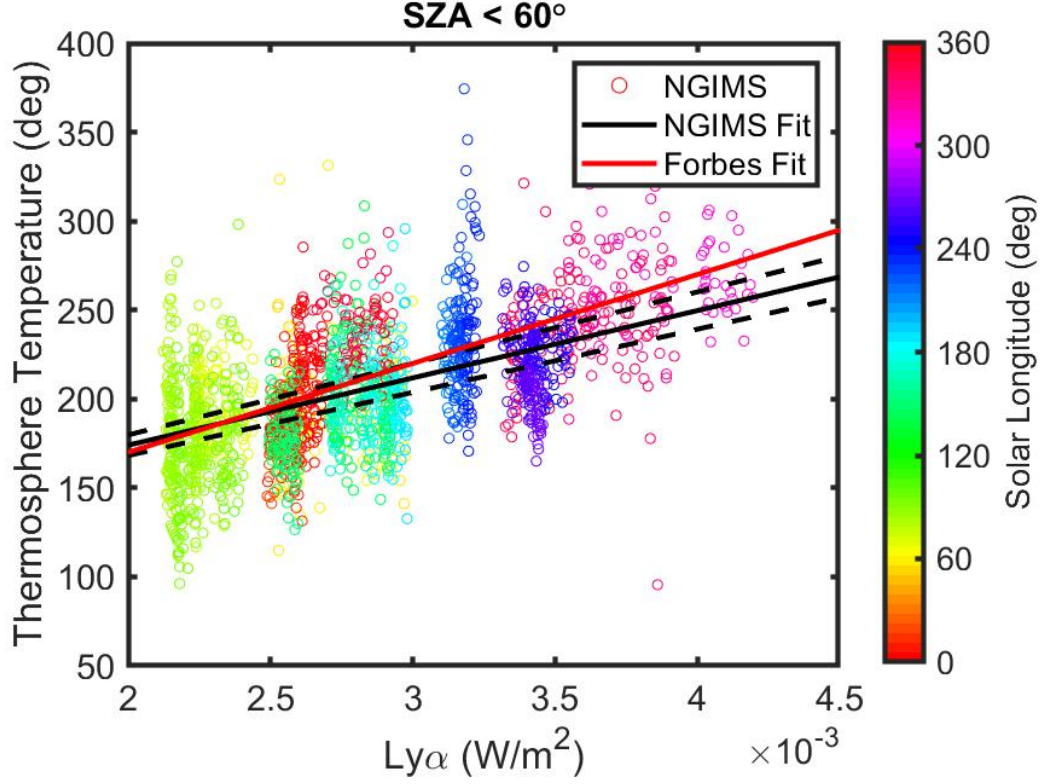
Figure 1. NGIMS scale height exospheric temperatures versus Lyman-α index (measured at Mars by EUVM) over the entire MAVEN mission (SZA=0-60 deg, LT = 6-18). Both MGS (Forbes Fit, solid red curve) and NGIMS (NGIMS Fit, solid black curve) trends are provided for comparison of solar cycle trends for # 23 and 24, respectively. The open circles denote the individual NGIMS orbit exospheric temperature values, color coded by season (Ls). The dashed curves represent the uncertainty of the NGIMS linear fit due to the errors in the scale height temperatures themselves. These errors are larger for solar high conditions.

ation in extracted Texo values about the linear trend is observed at all seasons. This variability seen in the reconstructed temperatures is mainly due to the presence of GWs, and this is fully consistent with the uncertainty of the scale height extraction fits and associated temperatures (approximately ± 50 K) as shown in Figure 1. This gravity wave variation is stochastic in nature.

In addition, an empirical trend using MGS Texo values (Forbes et al., 2008) and a similar (Mars based) Lyman-α index (now for SC23) is shown (red curve) for comparison to MAVEN. This MGS linear regression is calculated using an excellent database of Lyman-α fluxes obtained at Earth (LISIRD)(Machol et al., 2019), scaled by the Mars heliocentric distance, and rotated to Mars for this MGS sampling period (1-February 1999 to 7-July 2005). Corresponding Texo values are obtained from the MGS Precise Orbit Determination (POD) technique used to extract densities and derive Texo values at $\sim$390 km (Forbes et al., 2008). Endpoints near aphelion/solar minimum and perihelion/solar maximum conditions were utilized in computing this MGS regression (2.0 to 4.5 mWm^{-2}, the same as used for the NGIMS dataset). The resulting ΔTexo/ΔEUV sensitivities that emerge from these two linear regressions are as follows: $\sim$45$\pm$1.0 K m^2 mW^{-1} and $\sim$38$\pm$3.4 K m^2 mW^{-1} for MGS and MAVEN, respectively. It is notable that a small temperature offset exists between these MAVEN and MGS trend curves. This small discrepancy between their computed sensitivities (ΔTexo/ΔEUV) suggests differences in heat balance physics in the Mars dayside thermosphere during SC23 and SC24 (i.e. MGS versus MAVEN sampling periods). The major difference in the two datasets is that the EUV heating is likely larger as MGS mean Texo values approach $\sim$300K, while those for MAVEN approach $\sim$260K. This 40 K difference is due to the fact that SC23 period is more robust (active) than SC24. See a summary of solar cycle activity in Table 2.

The EUVM solar occultation (terminator) derived (ΔTexo/ΔEUV) sensitivities in Table 3 are about a factor of 1.3-1.5 smaller than those corresponding ones for MGS and MAVEN (E. M. Thiemann et al., 2018). These tabulated EUVM values are corrected for the Lyman-α index instead of the original integrated EUV flux index (0-94-nm). This Table 3 comparison suggests that dawn and dusk terminator heat balances may be different from those at low SZAs explored in this paper. This is to be expected since the solar EUV control of the high SZA (terminator) region is likely weaker than that at low SZAs (0-60°). In fact, dynamical influences may also play a role in terminator heat balances (Pilinski et al., 2018).

Table 2. Solar Cycle 21, 22, 23 and 24 indices at Earth for comparison of proxies indicating changing solar EUV-UV fluxes over time. Taken from monthly averaged peak values archived in the LISIRD database at LASP. PVO refers to Pioneer Venus Orbiter sampling, 1979-1992. MGS refers to Mars Global Surveyor sampling, 1999-2005. MVN coincides with the first 3- Mars years of MAVEN sampling, 2014-2019. Units of Lyman-α fluxes are mW m^{-2}.

Solar Cycle #	Sunspot #	F10.7-cm	Lyman-α
21 (PVO)	184	229	9.82
22 (PVO)	218	247	10.3
23 (MGS)	175	236	9.94
24 (MVN)	94	154	8.3

Table 3. Mars ΔTexo vs ΔEUV sensitivities from MGS and MAVEN sampling for SC#23 and SC#24, respectively. The EUVM solar occultation sensitivity is converted from an integrated EUV flux index (0-94-nm) to the Lyman-α index, and provides a mean value independent of dawn or dusk location. Finally, the PVO based Venus sensitivity is presented spanning SC#21. The $\pm$ values indicate the uncertainty in the fits (computed slopes) due to uncertainty in the solar fluxes and/or the temperature measurements themselves.

Mission (instrument)	Solar Cycle (MY)	ΔTexo/ΔEUV
MGS (POD)	23 (MY24-27)	45.0$\pm$1.0
MAVEN (NGIMS)	24-25 (MY32-35)	38.0$\pm$3.4
MAVEN (EUVM-SO)	24-25 (MY33-35)	30.0$\pm$1.4
PVO (ONMS and OUVS)	21	17.5$\pm$4.2

Figure 2 presents NGIMS scale height detrended temperatures versus SZA over the same ~12000 orbits of the MAVEN mission. Both morning (LT = 6-12) and afternoon (LT = 12-18) sector temperatures (SZA = 0-90°) are combined and colored coded to illustrate Ls (seasonal) behavior. The solar cycle trend line from Figure 1 is removed, yielding this detrended exospheric temperature behavior as a function of SZA. This new detrended curve is further characterized using a 20-degree moving average (black curve). It is evident that a ~25°K drop in running mean exospheric temperature over the dayside (from SZA = 0° to the terminators) is present in this NGIMS dataset. Furthermore, two SZA bins are selected to highlight SZA behavior: 0-60°, 60-90°. For SZA = 0-60°, the temperature variations are weakest (±5-10° K) about the zero line. Most importantly, the large scatter in temperatures seen in Figure 1 still exists in the NGIMS scale height temperature data in Figure 2, once the solar cycle linear trend is extracted and temperatures are organized in SZA. This remaining scatter (up to ±50 K FWHM) is similar to the typical NGIMS scale height temperature uncertainty of ±50 K over 0-60 SZA outlined above in Table 1. This variability still seen in both EUV and SZA sorted datasets is mainly due to the presence of gravity waves, which are stochastic in nature. The difference between afternoon (LT = 12-18) and morning (LT = 6-12) sensitivities is given in Figure 3 (see discussion below).

Figure 2 also shows that the variability of individual orbit Texo values about the 20-degree moving average increases as SZA = 90° is approached. This clearly reveals that the smallest variations are realized at low SZA (0-60°), presumably where the solar EUV heating maintaining temperatures is the strongest. Once again, as the terminator is approached, other factors play a larger role in the control of topside thermospheric temperatures (i.e. global winds, gravity and planetary waves, etc.). See Pilinski et al. (2018).

4.2 Comparison of the two NGIMS Texo methods of extraction

NGIMS dayside exospheric temperatures are plotted versus the EUVM Lyman-α index in Figure 3 for 8-specified periods (campaigns) over the MAVEN mission for SZA = 0-60° (see section 2.2.2 and Table 1). The hydrostatic integration method is applied here for Texo extraction over CO_2 densities spanning 10^8 to 10^7 cm^{-3}. Mean Texo values (black dots) plus 1-σ variations (vertical bars) are illustrated for these 8-campaigns. In addition, the NGIMS scale height temperature trend is extracted (dashed curve) from Figure 1 (LT = 6-18) and contrasted (solid curve) with a second trend (LT = 12-18) for

–18–
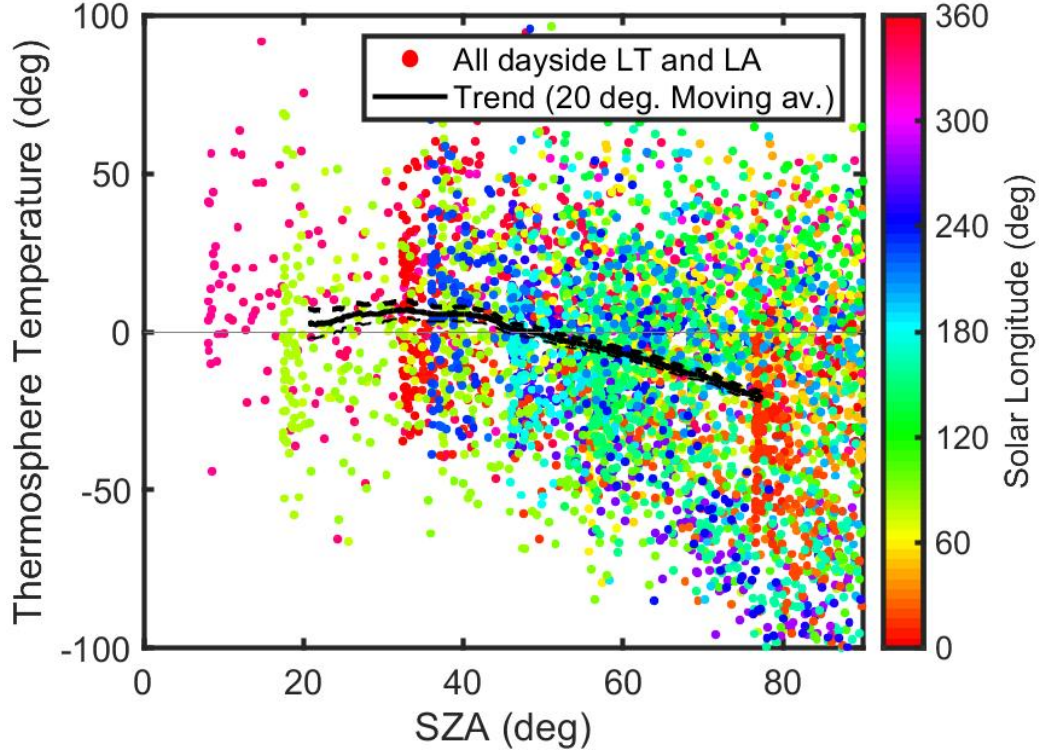
Figure 2. Both morning (LT = 6-12) and afternoon (LT = 12-18) sector (SZA = 0-90°) temperatures are combined and colored coded to illustrate Ls (seasonal) behavior. The solar cycle MAVEN trend line from Figure 1 is removed, yielding this detrended exospheric temperature behavior as a function of SZA. The dashed curves represent the errors to this trend owing to the errors in the scale height temperatures themselves. LT refers to Local Solar Time; LA refers to Latitude.
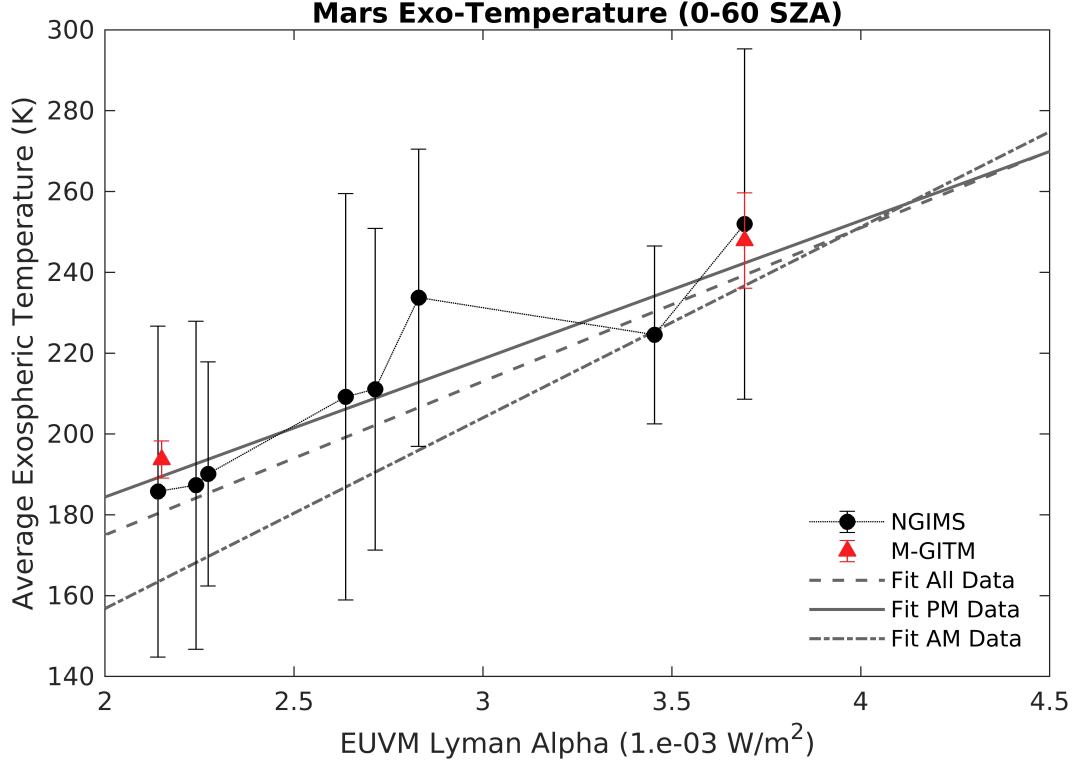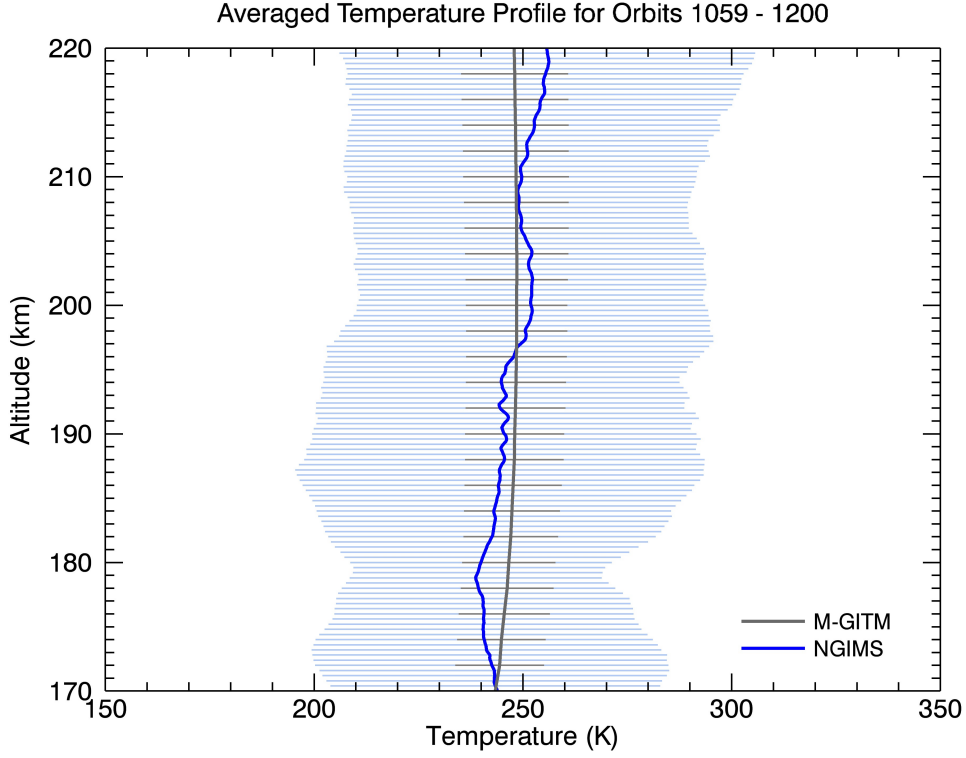
Figure 3. NGIMS dayside exospheric temperatures versus EUVM Lyman-α index are illustrated for 8-specified periods over the MAVEN mission for SZA = 0-60° (see Table 1). Black dots correspond to hydrostatic integration estimates of period averaged Texo values, with uncertainty bars added to denote 1-σ orbital variations about the mean. An NGIMS full dayside scale height trend is plotted (dashed curve) from Figure 1 (LT = 6-18) and contrasted (solid curve) with a second trend (LT = 12-18) for afternoon conditions only. Finally, a third trend (LT = 6-12) for morning conditions is displayed. Notice that full dayside and afternoon trends are similar, while that for morning conditions is cooler, especially for Lyman-α fluxes less than 3.5 mW/m2. M-GITM simulated mean Texo values (red triangles, plus 1-σ orbital variations about the mean) are also plotted for DD2E and PC19 intervals.

afternoon SZA conditions only. Finally, a third curve is added to illustrate morning (LT = 6-12) temperatures, now enabling comparison of afternoon versus morning temperature variations.

This figure illustrates that exospheric temperatures extracted by the hydrostatic integration method correspond closely to the linear trend derived from the scale height method (afternoon conditions) for extreme solar minimum to solar maximum conditions. Table 1 also specifically compares 8-period values of scale height temperatures and corresponding hydrostatic integration method derived values, revealing agreement within about $\pm$ 6 K throughout SC24. Notably, Texo values for periods #2 and 3 (i.e. from both techniques) show departures from the linear trend. Period #3 may be associated with non-solar forcing during the mid-decay phase of the regional C-dust storm in MY33. Indeed, warmer thermosphere temperatures have been inferred during this dust event (e.g. Fang et al., 2020). Nevertheless, the overall strong linear trend suggests that the scale height method can be applied for general usage to extract Mars dayside exospheric temperatures. Moreover, the afternoon extracted temperatures are $\sim$10-25 K warmer than those extracted over morning local times for Lyman-α fluxes less than 3.5 mW/m^2. This trend of warmer afternoon topside thermosphere temperatures is observed in other MAVEN datasets (e.g. Jain et al., 2021) and predicted by pre-MAVEN model simulations (e.g. Bougher et al., 2015).

4.3 Study of two temperature extreme cases: DD2E plus PC19 periods

It is instructive to investigate the performance of the M-GITM code for capturing the MAVEN solar cycle trend of dayside Texo illustrated in Figure 3. The goal is to determine the underlying heat balances that are required to reproduce observed Texo variations over the solar cycle. We have selected two extreme cases for conducting new M-GITM simulations in this paper. These cases are found in Table 1 as follows: (Period 1) a solar maximum/near-perihelion case capturing extended Deep Dip 2 conditions early in the MAVEN mission (2015), and (Period 8) a solar minimum/aphelion case appropriate to post-solar conjunction conditions (late 2019). M-GITM outputs from these two cases are extracted along the NGIMS sampling trajectories appropriate to deep dayside conditions (SZA $\leq$ 40 degrees). Interpolation is conducted from the model's coarse nominal grid to the location of each NGIMS sampling location. This is in effect a flythrough of the M-GITM model output along the NGIMS orbit trajectory. Mean temperatures

–21–

Figure 4. NGIMS and M-GITM dayside exospheric temperatures during the extended DD2 campaign are illustrated (see Table 1, first campaign). Mean NGIMS extracted temperatures (dark blue curve) are surrounded by cross-hatched (light blue) lines indicating 1σ orbital variations about the mean. A mean temperature of 252±43.3K is derived over 200-220 km. Corresponding M-GITM campaign mean temperatures (solid black curve) are presented for a standard gravity wave case. Here, the computed mean temperature (over 200-220 km) is 248±12K.

493 and their 1-σ orbital variations throughout the campaign about the mean are plotted
494 in Figure 3 for both the NGIMS and M-GITM profiles.

495 It is noteworthy that standard Mars gravity wave parameters are used for the mo-
496 mentum and energy deposition code that is incorporated within these M-GITM simu-
497 lations and utilized for these two extreme cases (Roeten et al., 2022). The correspond-
498 ing momentum deposition was previously found to impact the $\sim$90-160 km region of the
499 simulated thermosphere, thereby slowing winds by up to a factor of 2, reducing the day-
500 to-night transport of atomic O (leaving more on the Mars dayside), and ultimately pro-
501 viding enhanced CO_2 15-μm cooling in the lower dayside thermosphere (Roeten et al.,
502 2022). See section 3.

503 Figure 4 shows both mean DD2 temperature profiles over 170 to 220 km, demon-
504 strating that the simulated (M-GITM) and measured (NGIMS) mean profiles match very
505 well. The model 1-σ values in Figure 4 (black horizontal bars) represent the dispersion
506 of the Texo values about the computed mean. Similarly, the blue cross hatched bars rep-
507 resent the 1-σ variability of the NGIMS (hydrostatic method) derived Texo values about
508 the mean. The measured exosphere temperature of 252$\pm$43.3K is quite close to the cor-
509 responding computed mean temperature of 248$\pm$12K over 180-200 km. Notice that the
510 real atmosphere orbital 1σ temperature variability is much larger (factor of $\sim$3.5) than
511 that calculated by M-GITM. This is largely because M-GITM is a climate model that
512 does not capture all the gravity, planetary and tidal waves that contribute to orbit-to-
513 orbit variability that is present in the real atmosphere. Specifically, modern M-GITM
514 simulations utilizing the new gravity wave formulation (see section 3) are able to cap-
515 ture the mean impacts on winds and temperatures, but not the individual impacts of grav-
516 ity waves launched upward and breaking at thermospheric heights. M-GITM cannot cap-
517 ture this large stochastic variability due to gravity waves observed in NGIMS Texo val-
518 ues illustrated in Figure 4. However, the variability that is captured by M-GITM includes
519 changes in the evolving orbital trajectories over $\sim$140 orbits, plus the changing solar fluxes
520 (EUVM provided) that are used to drive the EUV heating simulated by M-GITM.

521 Figure 5 illustrates the heat balance terms that maintain the simulated DD2 ex-
522 tended mean temperature profile of Figure 4. The altitude scale covers 135 to 220 km
523 in order to capture the CO_2 15-μm cooling layer that peaks near 150 km. Notice that
524 molecular thermal conduction largely balances EUV heating above $\sim$150 km (approx-
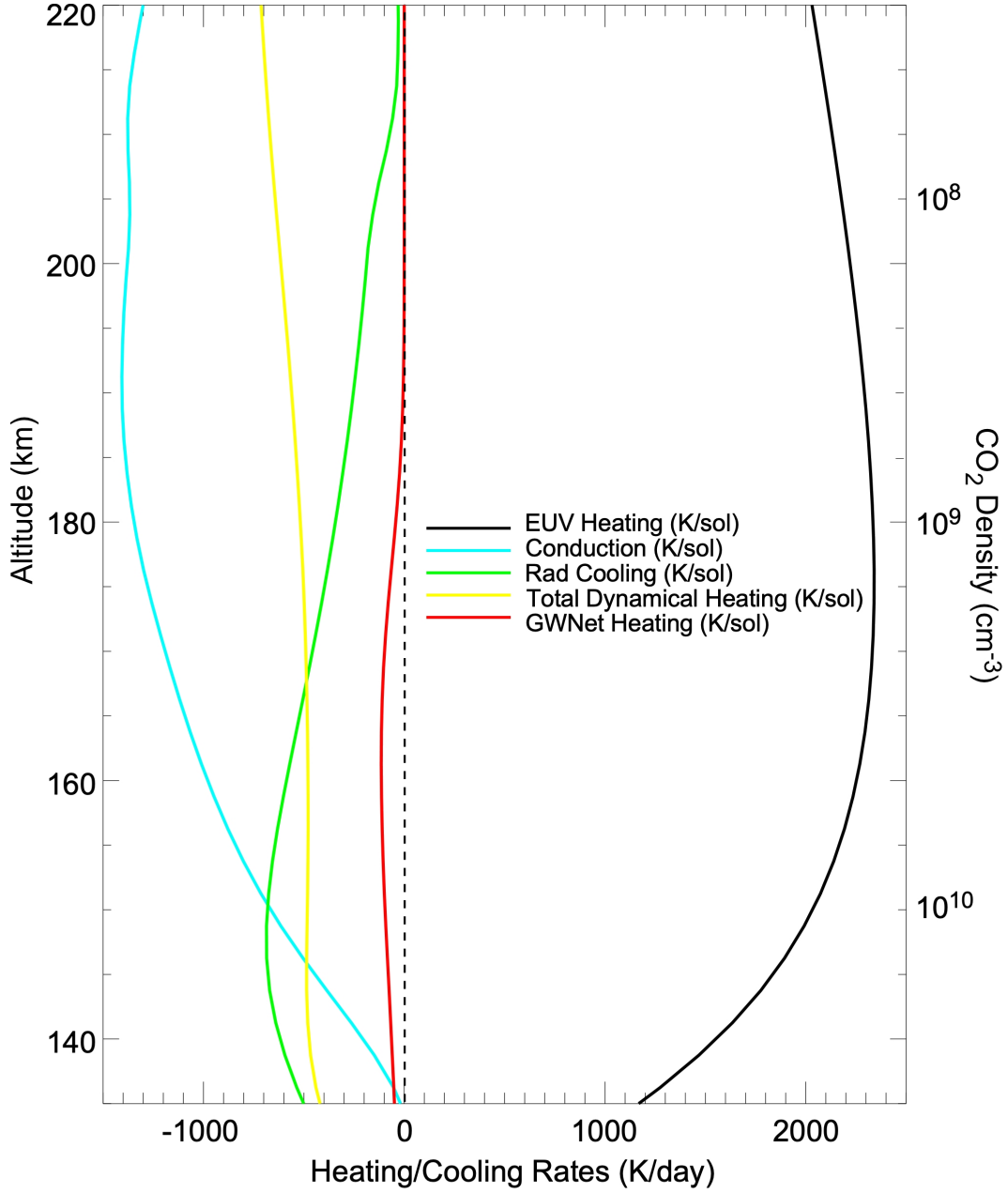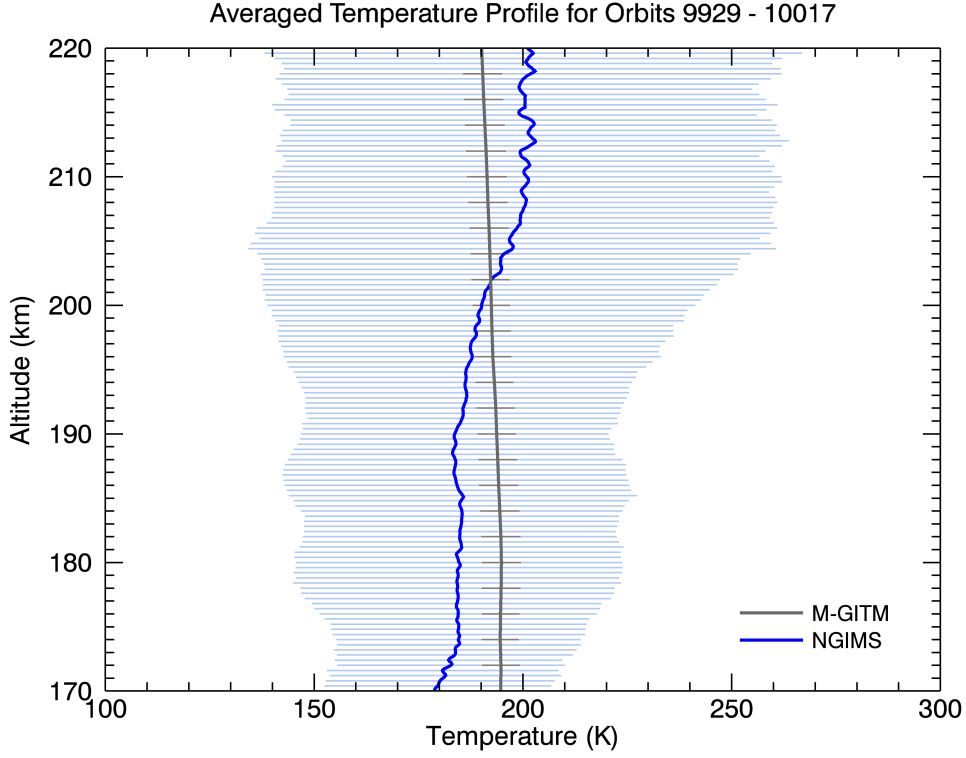
Figure 5. M-GITM extracted heat balances terms are provided for the DD2 extended campaign, corresponding to the mean computed temperature profile from Figure 4. This is the extreme case where solar maximum - post-perihelion conditions prevailed. The averaged EUV solar forcing over this DD2 extended campaign is used to select a corresponding specific orbit to yield a set of campaign averaged heat balance terms for plotting. Altitudes span ∼135 to 220 km (above the near IR heating layer). Terms include: EUV heating (EUVHeating), CO_2 15-μm cooling (Radcooling), molecular thermal conduction (Conduction), net dynamical heating (TotalDynamicalHeating), and gravity wave net heating (GWNetHeating). Units are K/day (Earth day).

imately where the CO_2 density is 10^{10} cm^{-3}), while CO_2 15-μm cooling plus net dynamical cooling (i.e. adiabatic cooling due to upwelling winds) together dominate cooling below 150 km. It is also evident that net gravity wave cooling (i.e. owing to gravity energy deposition effects) approaches $\sim$100 K/day near 160 km, but is otherwise negligible in its net impact on the heat budget. Thus, for solar maximum conditions, molecular conduction is not the dominant cooling mechanism at all altitudes. Rather, the emission of CO_2 15-μm photons to space provides thermosphere cooling that plays an important role in radiating away the heat conducted downward to lower thermospheric altitudes. Will this modest CO_2 15-μm cooling effect also hold for solar minimum/aphelion conditions when thermospheric temperatures are cooler? PC19 simulations below will answer this question.

Figure 6 illustrates both mean PC19 temperature profiles over 170 to 220 km, showing that the simulated (M-GITM) and measured (NGIMS) profiles match reasonably well. Nevertheless, the measured exosphere temperature of 185±40.9 K is a bit cooler than the corresponding computed mean temperature of 193.7±4.6K over 180-200 km. In addition, there is a slight cooling of the computed mean temperature profile with increasing altitude, that corresponds to dynamical cooling (upwelling flow) that contributes near 200 km (see Figure 7). More importantly, the real atmosphere orbit-to-orbit 1σ temperature variability is much larger (factor of $\sim$9) than that calculated by M-GITM. This discrepancy is even larger than for DD2 conditions (see Figure 4). Indeed, the solar forcing (EUV heating) for PC19 conditions is much weaker than for DD2 conditions (see Figure 5). This implies that the impacts of upward propagating waves (i.e. tides, planetary, and gravity waves) will be larger for PC19 than for DD2 conditions. For instance, the larger impact of tidal forcing at lower thermospheric altitudes during solar minimum conditions is clearly observed using IUVS measurements (see Jain et al. (2021) and Thaller et al. (2021)). These NGIMS solar minimum temperatures (and their 1-σ temperature variability) provide further support for this claim of stronger wave activity impacts during solar minimum conditions.

Figure 7 illustrates the heat balance terms that maintain the simulated PC19 extended mean temperature profile of Figure 6. Notice that molecular thermal conduction largely balances EUV heating over nearly the entire domain ($\sim$135-210 km), while dynamical cooling plays a stronger role at higher altitudes. Notably, CO_2 15-μm cooling is not important anywhere in this altitude region. It is also evident that net gravity wave

–25–

Figure 6. NGIMS and M-GITM dayside exospheric temperatures during the extended PC19 campaign are illustrated (see Table 1, last campaign). Mean NGIMS extracted temperatures (dark blue curve) are surrounded by cross-hatched (light blue) lines indicating 1σ orbital variations about the mean. A mean temperature of 185 ± 40.9 K is derived over 180-200 km. Corresponding M-GITM campaign mean temperatures (solid black curve) are presented for a standard gravity wave case. Here, the computed mean temperature (over 180-200 km) is 193.7 ± 4.6K.
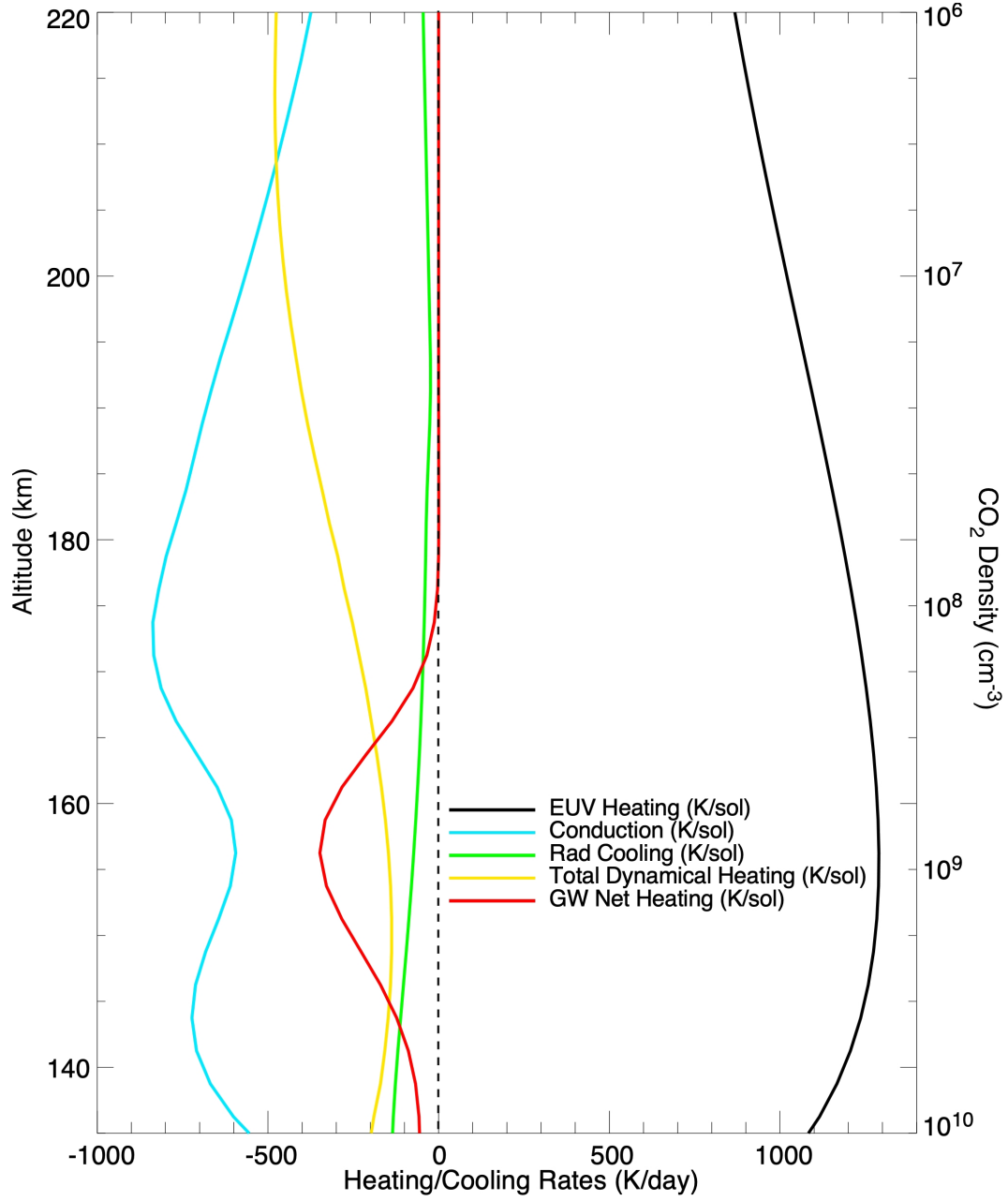
Figure 7. M-GITM extracted heat balances terms are provided for the PC19 campaign, corresponding to the mean computed temperature profile from Figure 6. This is the extreme case where solar minimum - aphelion conditions prevailed. Altitudes span ∼130 to 220 km (above the near IR heating layer). Notice the revised CO_2 density vertical scale here, in contrast to that for DD2E in Figure 5. Terms include: EUV heating (EUVHeating), CO_2 15-μm cooling (Radcooling), molecular thermal conduction (Conduction), net dynamical heating (TotalDynamicalHeating), and gravity wave net heating (GWNetHeating). Units are K/day (Earth day).
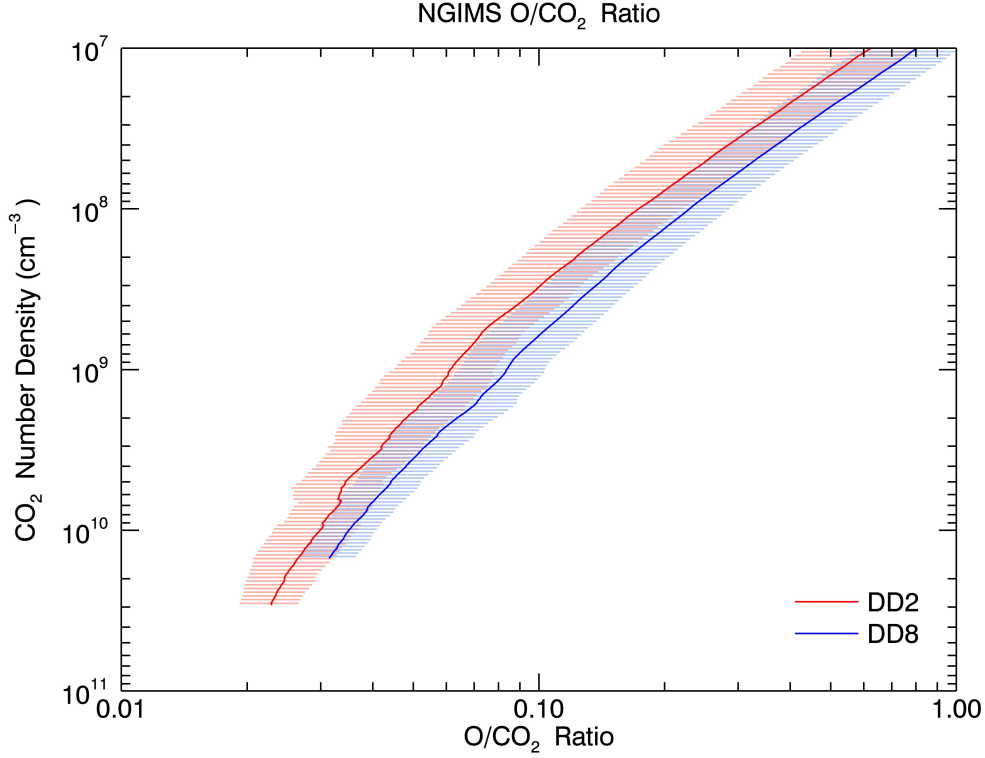
Figure 8. NGIMS O abundance profiles for both DD2 and DD8 conditions. Orbit to orbit 1-σ variations about the mean are also plotted as cross-hatched lines. Plotted vertical coordinate is CO_2 density (cm^{-3}). There is a close match of M-GITM and NGIMS O/CO_2 ratios about 1-scale height above the peak CO_2 cooling layer, but larger ratios are computed by M-GITM than observed at higher altitudes, where CO_2 cooling has negligible impact on the heat budget for solar high and low conditions.

558 cooling (i.e. owing to gravity energy deposition effects) approaches $\sim$300 K/day over $\sim$150-

559 165 km. This value is larger than for DD2 conditions, indicating that GW effects are more

560 pronounced in the solar minimum thermosphere than for solar maximum. Nevertheless,

561 the net impact on the overall heat budget is still small. Thus, for solar minimum con-

562 ditions, molecular conduction is mostly dominant as a cooling mechanism at altitudes

563 below $\sim$ 205 km, while CO_2 15-μm cooling is weak. This is much different than com-

564 puted for solar maximum conditions as seen in Figure 5. Why is this so?

565   Figure 8 shows NGIMS extracted profiles of O abundances (i.e. O/CO_2 ratios) for

566 both DD2 and DD8 Deep Dip campaign periods (see Table 1). In addition, 1-σ orbital

variations about the mean O/CO_2 profiles are provided as cross-hatched lines. It is noted that DD8 is used as a proxy for PC19, since derived exospheric temperatures are very similar (see Table 1), and DD8 extends to lower periapsis altitudes where O abundances are available for study. These are new MAVEN measurements spanning the solar cycle that help to constrain the CO_2 cooling rates at Mars for the first time.

The comparison here between DD2 and DD8 abundances (over solar high to solar low conditions) shows that at the common highest CO_2 density of $\sim 10^{10}$ cm^{-3} the O/CO_2 ratios are much the same ($\sim$ 0.03-0.035). This corresponds to $\sim$150 km and $\sim$135 km for DD2 and DD8 sampling, respectively. In addition, this implies that the collision of O atoms with CO_2 molecules for enhancing Mars CO_2 15-μm cooling is similarly efficient during both solar low and solar high conditions in the lower thermosphere (Huestis et al., 2008). Nevertheless, the magnitude of CO_2 15-μm cooling is greatly reduced for solar minimum conditions (see Figure 7). This is due to the much weaker solar EUV forcing and resulting cooler temperatures at these PC19 thermospheric altitudes. Recall that CO_2 cooling is highly non-linearly temperature dependent (Huestis et al., 2008; S. W. Bougher et al., 1994).

Table 4 provides a detailed comparison between NGIMS (measured) and M-GITM (computed) O/CO_2 ratios for these DD2 and DD8 sampling periods. These Deep Dip campaign values are displayed at a constant CO_2 density (where CO_2 15-μm cooling peaks) to best illustrate variations that are driven by in-situ thermospheric drivers, and not hydrostatic variations linked to the changing seasons. Results show a reasonble comparison for DD2 conditions in the lower thermosphere (equivalent to $\sim$ 145 km) where CO_2 cooling dominates. Likewise, a good comparison for DD8 conditions also appears in the lower thermosphere (equivalent to $\sim$135-138 km) where CO_2 cooling peaks but does not dominate the heat budget. This reasonable data-model match of O/CO_2 ratios in the lower thermosphere supports our finding that CO_2 15-μm cooling does play a modest role in regulating the heat budget in the Mars thermosphere for solar high conditions. However, CO_2 cooling does not play any significant role in balancing EUV heating for solar low conditions at Mars. This CO_2 thermostatic cooling effect is much weaker at Mars than for Venus (see section 5).

–29–

Table 4. Comparison between NGIMS (measured) and M-GITM (computed) O/CO_2 ratios for DD2 and DD8 sampling periods in the lower thermosphere.

CO_2 Density($\#/cm^3$) (altitude)	Period	NGIMS	M-GITM
10^{10} ($\sim$150 km)	DD2 (only)	0.032	0.050
10^{10} ($\sim$135 km)	DD8	0.035	0.040

5 Broader Implications: Comparative Planetology

Previously, the role of CO_2 15-μm cooling was found to be substantially different for the simulated 3-D model heat budgets of the upper atmospheres of Venus, Earth, and Mars (e.g. S. W. Bougher et al., 1994; Bougher et al., 1999, 2000; Huestis et al., 2008). In light of the new findings from MAVEN for Mars (above), how does the new MAVEN derived dayside temperature sensitivity (ΔTexo/ΔEUV) compare to that at Venus, another CO_2 dominated planet? This sensitivity comparison can now be made using measured solar Lyman-α fluxes obtained in-situ at Venus and Mars for the first time. It is also important to constrain the relative role of O enhanced CO_2 15-μm cooling at Mars in the context of its much different (unique) role at Venus, especially that measured O abundances in the dayside thermospheres of both planets are now available.

The photo-electron current (Ipe) from the Pioneer Venus (PV) Orbiter Electron Temperature Probe (OETP) (Brace et al., 1988), when measured outside the atmosphere, was found to be generated by the solar EUV-UV flux spanning wavelengths ranging from about 55.0 to 130.0-nm. Approximately 51% of the spectral contribution for Ipe comes from Lyman-α. This Ipe was calibrated to total solar EUV flux and Lyman-α flux by Brace et al. (1988). Correspondingly, one estimate of the dayside exospheric temperature over the solar cycle was made by fitting 39-orbits of PV-Orbiter Ultraviolet Spectrometer (OUVS) Lyman-α limb profiles with a model for 3-hydrogen components, one of which was a cold component (thermal hydrogen) whose temperature was adjusted to provide a best fit. The trend of increasing temperature with the advance of the solar cycle (minimum to maximum) was clearly derived, with a relative temperature change of about 80 K. Alternatively, empirical models and various datasets (Fox & Bougher, 1991; Kasprzak et al., 1997) estimate a relative temperature change up to 70 K over the so-

–30–

621 lar cycle. Thus, we have a measure of dayside exospheric temperature variation at Venus,

622 spanning solar cycle #21 (SC21), that can be linearly fit to the changing Lyman-α flux

623 measured at Venus.

624 The resulting SC21 Venus dayside temperature sensitivity (ΔTexo/ΔEUV) is about

625 $\sim$17.5$\pm$4.2 K m^2 mW^{-1}. This Venus sensitivity approaches $\sim$40-50% of that derived from

626 MAVEN NGIMS and MGS POD values (see Table 3). This is a revised calculation for

627 Venus sensitivity based upon Lyman-α fluxes received at the planet. This sensitivity com-

628 parison between Venus and Mars now approaches a factor of 2-3 enhancement for Mars,

629 in contrast to a factor of 5 computed previously using F10.7-cm fluxes as the solar in-

630 dex (Forbes et al. 2008). Why are these sensitivities so different for Venus and Mars even

631 though both are CO_2 dominated planets?

632 S. Bougher et al. (1999) and Bougher et al. (2008) make use of the Venus Ther-

633 mospheric General Circulation Model (VTGCM) to compute the solar minimum to max-

634 imum dayside temperature profiles, and correctly captures the measured exospheric tem-

635 perature changes over the solar cycle. The underlying thermal balances suggest that CO_2

636 15-μm emission is the dominate cooling mechanism that balances the peak of the EUV

637 heating layer near $\sim$150 km (approximately where the CO_2 density is $\sim$10^{10} cm^{-3}). Fur-

638 thermore, this strong cooling is regulated by enhanced O/CO_2 ratios measured at so-

639 lar maximum (SC21) by the ONMS instrument ($\sim$65%) which are much larger than cor-

640 responding O/CO_2 ratios at Mars (3-5%) at the same constant CO_2 density level. In essence,

641 a CO_2 cooling thermostat is in operation at Venus that is very efficient at regulating day-

642 side temperatures over the solar cycle. By contrast, Mars O/CO_2 ratios are much smaller

643 and the O-CO_2 enhancement of CO_2 15-μm cooling is much weaker than at Venus. In-

644 stead, molecular thermal conduction is simulated to balance the bulk of the dayside EUV

645 heating at Mars.

6 Summary and Conclusions

647 MAVEN NGIMS measured dayside exospheric temperatures (SZA$\leq$ 60 degree) are

648 shown to vary by up to $\sim$80 K ($\sim$180-260 K) over solar cycle # 24 (SC24). This linear

649 least squares empirical trend corresponds to an EUV sensitivity (ΔTexo/ΔEUV) of $\sim$38

650 K m^2 mW^{-1}. Lyman-α fluxes are used in this calculation for computing the EUV sen-

651 sitivity.

–31–

This MAVEN dayside sensitivity (ΔTexo/ΔEUV) is slightly smaller than that derived from MGS solar cycle #23 (SC23) measurements (45 K m^2 mW^{-1}). The main difference between the two is that SC23 is much stronger than SC24, so that enhanced EUV heating drives the maximum MGS measured dayside exospheric temperature to be closer to 300 K. This larger range of EUV fluxes and resulting heating is consistent with the SC23 dayside exospheric temperature variation that is larger (i.e. $\sim$180 to 300 K) (Forbes et al., 2008; Bougher et al., 2009).

It is determined that SC24 dayside exospheric temperatures derived from both the scale height and the hydrostatic integration methods yield similar topside values. Temperatures are extracted over 180-200 km for solar low conditions, and 200-220 km for solar high conditions. This implies that scale height temperatures, which are fast to calculate, can be used reliably to derive topside temperatures mission-wide for statistical analysis. Alternatively, the hydrostatic integration method is needed for detailed studies for which profiles are required.

Useful comparisons of MAVEN IUVS exosheric temperatures (Texo) and their variations over solar cycle, seasons and local time (Jain et al. 2021) can be made with these new NGIMS measurements. First and foremost, the long term variations in dayside Texo are largely driven by solar EUV and seasonal variations as shown in both IUVS and NGIMS measurements, as expected. The $\sim$180 to 260 K mean Texo variation derived from NGIMS scale height and hydrostatic methods is quite close to the IUVS variation of 175 to 250 K (Jain et al. 2021). The latter is derived from scale heights gleaned from CO_2^+ Ultraviolet doublet emission profiles. In addition, particular attention was given to solar minimum conditions and associated Texo variations for these IUVS studies. Seasonal variations (perihelion to aphelion) of Texo were shown to vary from 175 to 220 K (Jain et al. 2021). Solar low conditions defined for these NGIMS studies (i.e. Lyman-α fluxes less than 3.5 mW/m^2) constrained similar seasonal variations to be 185 to 230 K. Finally, IUVS studies concluded that Texo values are highly variable with respect to local time when solar forcing, Mars-sun distance and dust effects are removed (Jain et al. 2021). Similar constraints are found in NGIMS data for the extreme aphelion/solar low conditions (see Figure 3). Here morning and afternoon Texo values vary by up to $\sim$30 K (for SZA $\leq$ 60). This value is comparable to $\sim$50 K for a wider range (SZA $\leq$ 85) of IUVS dayside conditions. In short, for these three dayside thermospheric features, IUVS and NGIMS measurements for Texo are complementary and generally consistent.

–32–

M-GITM has been used to simulate extreme MAVEN cases (DD2E and PC19), corresponding to solar high and low conditions, respectively. Mean temperature profiles and corresponding heat balances are computed for interpreting the extreme dayside exospheric temperatures shown in Figure 3. It is shown that the primary dayside EUV heating is largely balanced by molecular thermal conduction throughout SC24. However, CO_2 15-μm cooling does play a modest role in regulating the heat budget in the Mars thermosphere for solar high conditions. This occurs as dayside thermal conduction transfers EUV heat to lower altitudes below $\sim$150 km (i.e. for CO_2 densities higher than 10^{10} cm^{-3}) where 15-μm emission largely provides NLTE cooling to space. CO_2 15-μm cooling does not play any appreciable role for solar low conditions. The global winds also contribute mildly to dayside cooling at low SZA, owing in part to adiabatic cooling due to upwelling winds and also horizontal transport from divergent flow.

From a comparative planetology perspective, the MAVEN newly derived dayside temperature sensitivity (ΔTexo/ΔEUV) can be contrasted to that computed at Venus from measurements obtained during the Pioneer Venus (PVO) mission. Furthermore, CO_2 cooling rates can be constrained for both planets now that measured O abundances in their dayside thermospheres are now available for the first time. These solar cycle #21 (SC21) measurements make use of both PV-OUVS exospheric temperature measurements ($\sim$250-330 K), and PV-ONMS measurements as well as in-situ solar Lyman-α fluxes derived from the photo-electron current of the PV-OETP instrument. The resulting SC21 Venus dayside temperature sensitivity (ΔTexo/ΔEUV) is about $\sim$17.5 K m^2 mW^{-1}, which is about $\sim$40-50% of that derived from MAVEN NGIMS (SC24) and MGS (SC23) values. This sensitivity comparison between Venus and Mars now approaches a factor of 2-3 enhancement for Mars, in contrast to a factor of 5 computed previously using F10.7-cm fluxes as the solar index (Forbes et al. 2008). VTGCM model simulations suggest that the underlying thermal balances determine that CO_2 15-μm emission is the dominate cooling mechanism that balances the bulk of the EUV heating in the Venus thermosphere. This is in stark contrast to Mars, for which molecular thermal conduction is instead dominant and CO_2 cooling is much weaker. This explains why the temperature-EUV sensitivity (ΔTexo/ΔEUV) is larger for Mars than Venus. Furthermore, it yields a larger exospheric temperature variation over a robust solar cycle for Mars ($\sim$180-300 K) than for Venus ($\sim$250-330 K).

–33–

These conclusions serve to interpret the MAVEN NGIMS measurements in the context of previous Mars measurements from MGS and in light of other Pioneer Venus measurements. Dayside exospheric temperature variations for Venus and Mars are indeed controlled by their respective underlying thermal balances. However, the role of CO_2 15-μm cooling for each planet's thermosphere is much different, being much stronger for Venus than for Mars.

Acknowledgments

Open Research

The NGIMS densities and scale heights used for this study are available on the PDS (Benna & Lyness, 2014). These datasets are also discussed in the NGIMS Software Interface Specification (Benna & Elrod, 2020). The scale height temperatures are an NGIMS Level 3, Version 6, Revision 1 data product while the neutral densities are an NGIMS Level 2, Version 8, Revision 1 data product.

In addition, solar fluxes used for data analysis and model simulations are taken from the MAVEN/EUVM FISM-M empirical model corresponding to a Level 3, Version 14, Revision 3 data product on the PDS (Eparvier, 2022).

Finally, datacubes and orbital tables containing M-GITM computed outputs from simulations used in this study are available on the University of Michigan Deep Blue Data repository (S. W. Bougher & Roeten, 2022).

References

Benna, M., & Elrod, M. (2020). MAVEN Neutral Gas and Ion Mass Spectrometer (NGIMS) PDS Software Interface (SIS). , *Version 1.12*, DOC Number MAVEN-NGIMS-SIS-0001.

Benna, M., & Lyness, E. (2014). MAVEN Neutral Gas and Ion Mass Spectrometer Data [Dataset], NASA Planetary Data System. doi: doi.org/10.17189/1518931

Benna, M., Mahaffy, P. R., Grebowsky, J. M., Fox, J. L., Yelle, R. V., & Jakosky, B. M. (2015). First measurements of composition and dynamics of the Martian ionosphere by MAVEN's Neutral Gas and Ion Mass Spectrometer. *Geophysical Research Letters*, *42*(21), 8958-8965. doi: 10.1002/2015GL066146

Bougher, S., Keating, G., Zurek, R., Murphy, J., Haberle, R., Hollingsworth, J., et al. (1999). Mars Global Surveyor aerobraking : Atmospheric trends and model interpretation. *Advances in Space Research*, *23*, 1887. doi: 10.1016/S0273-1177(99)00272-0

Bougher, S. W., Blelly, P.-L., Combi, M., Fox, J. L., Mueller-Wodarg, I., Ridley, A., et al. (2008). Neutral upper atmosphere and ionosphere modeling. *Space Sci. Rev.*, *139*, 107-141. doi: 10.1007/s11214-008-9401-9

Bougher, S. W., Brain, D. A., Fox, J. L., Gonzalez-Galindo, F., Simon-Wedlund, C., & Withers, P. G. (2017). Upper Neutral Atmosphere and Ionosphere, in *The Atmosphere and Climate of Mars* (R. M. Haberle, R. T. Clancy, F. Forget, M. D. Smith, & R. W. Zurek, Eds.). Cambridge University Press. doi: 10.1017/9781139060172.014

Bougher, S. W., Engel, S., Roble, R. G., & Foster, B. (1999). Comparative terrestrial planet thermospheres 2. Solar cycle variation of global structure and winds at equinox. *J. Geophys. Res.*, *1041*, 16591-16611. doi: 10.1029/1998JE001019

Bougher, S. W., Engel, S., Roble, R. G., & Foster, B. (2000). Comparative terrestrial planet thermospheres 3. Solar cycle variation of global structure and winds at solstices. *J. Geophys. Res.*, *105*, 17669-17692. doi: 10.1029/1999JE001232

Bougher, S. W., Hunten, D. M., & Roble, R. G. (1994). CO2 cooling in terrestrial planet thermospheres. *J. Geophys. Res.*, *99*, 14609-14622. doi: 10.1029/94JE01088

Bougher, S. W., Jakosky, B. M., Halekas, J., Grebowsky, J., Luhmann, J. G., et al. (2015b). Early MAVEN dip deep campaign reveals thermosphere and ionosphere variability. *Science*, *350*, 1-7. doi: 10.1126/science.aad0459

Bougher, S. W., McDunn, T. M., Zoldak, K. A., & Forbes, J. M. (2009). Solar cycle variability of Mars dayside exospheric temperatures: Model evaluation of underlying thermal balances. *Geophys. Res. Lett.*, *360*, L05201. doi:

10.1029/2008GL036376

Bougher, S. W., Pawlowski, D., Bell, J. M., Nelli, S., McDunn, T., Murphy, et al. (2015). Mars Global Ionosphere-Thermosphere Model: Solar cycle, seasonal, and diurnal variations of the Mars upper atmosphere. *J. Geophys. Res.*, *120*, 311-342. doi: 10.1002/2014JE004715

Bougher, S. W., Roble, R. G., & Fuller-Rowell, T. (2002). Simulations of the upper atmospheres of the terrestrial planets. *Geophysical Monograph Series*, *130*, 261-288. doi: 10.1029/130GM17

Bougher, S. W., & Roeten, K. J. (2022). Mars thermospheric temperature and density distributions: M-GITM simulated datasets for comparison to MAVEN/NGIMS measurements [Dataset], University of Michigan - Deep Blue Data. doi: doi.org/10.7302/4rck-ds11

Bougher, S. W., Roeten, K. J., Olsen, K., Mahaffy, P. R., Benna, M., Elrod, M., et al. (2017). The structure and variability of Mars dayside thermosphere from MAVEN NGIMS and IUVS measurements: Seasonal and solar activity trends in scale heights and temperatures. *Journal of Geophysical Research: Space Physics*, *122*(1), 1296-1313. doi: 10.1002/2016JA023454

Brace, L. H., Hoegy, W. R., & Theis, R. F. (1988). Solar EUV measurements at Venus based on photoelectron emission from the Pioneer Venus Langmuir Probe. *J. Geophys. Res.*, *93*, 7282-7296. doi: 10.1029/JA093iA07p07282

Elrod, M. K., Bougher, S., Bell, J., Mahaffy, P. R., Benna, M., Stone, S., et al. (2017). He bulge revealed: He and CO2 diurnal and seasonal variations in the upper atmosphere of Mars as detected by MAVEN NGIMS. *Journal of Geophysical Research: Space Physics*, *122*(2), 2564-2573. doi: 10.1002/2016JA023482

Elrod, M. K., Bougher, S. W., Roeten, K., Sharrar, R., & Murphy, J. (2020). Structural and compositional changes in the upper atmosphere related to the PEDE-2018 dust event on Mars as observed by MAVEN NGIMS. *Geophysical Research Letters*, *47*(4), e2019GL084378. doi: 10.1029/2019GL084378

Eparvier, F. G. (2022). MAVEN EUV Modeled Data Bundle [Dataset], NASA Planetary Data System. doi: doi.org/10.17189/1414173

–36–

Fang, X., Bougher, S. W., Johnson, R. E., Ma, Y., & Liemohn, M. W. (2013). The importance of pickup oxygen ion precipitation to the Mars upper atmosphere under extreme solar wind conditions. *Geophys. Res. Lett.*, *40*, 1922-1927. doi: 10.1002/grl.50415

Fang, X., Ma, Y., Lee, Y., Bougher, S. W., Liu, G., Benna, M., et al. (2020). Mars dust storm effects in the ionosphere and magnetosphere and implications for atmospheric carbon loss. *J. Geophys. Res.*, *125*. doi: 10.1029/2019JA026838

Forbes, J. M., Lemoine, F. G., Bruinsma, S. L., Smith, M. D., & Zhang, X. (2008). Solar flux variability of Mars' exosphere densities and temperatures. *Geophysical Research Letters*, *35*(1). doi: 10.1029/2007GL031904

Fox, J. L. (2004). Response of the Martian thermosphere/ionosphere to enhanced fluxes of solar soft X rays. *Journal of Geophysical Research: Space Physics (1978–2012)*, *109*(A11). doi: 10.1029/2004JA010380

Fox, J. L., & Bougher, S. W. (1991). Structure, luminosity, and dynamics of the Venus thermosphere. *Space Sci. Rev.*, *55*, 357-489. doi: 10.1007/978-94-011-3300-5_7

González-Galindo, F., Chaufray, J.-Y., López-Valverde, M. A., Gilli, G., Forget, F., Leblanc, F., et al. (2013). 3D Martian Ionosphere model: I. The photochemical ionosphere below 180 km. *Journal of Geophysical Research*, *118*, 2105-2123. doi: 10.1002/jgre.20150

González-Galindo, F., López-Valverde, M. A., Forget, F., García-Comas, M., Millour, E., & Montabone, L. (2015). Variability of the Martian thermosphere during eight Martian years as simulated by a ground-to-exosphere global circulation model. *Journal of Geophysical Research: Planets*, *120*(11), 2020-2035. doi: 10.1002/2015JE004925

González-Galindo, F., Forget, F., López-Valverde, M., Angelats i Coll, M., & Millour, E. (2009). A ground-to-exosphere Martian general circulation model: 1. Seasonal, diurnal, and solar cycle variation of thermospheric temperatures. *Journal of Geophysical Research: Planets*, *114*(E4). doi: 10.1029/2008JE003246

Gupta, N., Rao, N. V., Bougher, S. W., & Elrod, M. K. (2021). Latitudinal and seasonal asymmetries of the helium bulge in the Martian upper atmosphere. *J. Geophys. Res. Planets*, *126*. doi: 10.1029/2021JE006976

Haberle, R. M., Joshi, M. M., Murphy, J. R., Barnes, J. R., Schofield, J. T., Wilson, G., et al. (1999). General circulation model simulations of the Mars Pathfinder atmospheric structure investigation/meteorology data. *Journal of Geophysical Research*, *104*, 8957-8974. doi: 10.1029/1998JE900040

Huestis, D. L., Bougher, S. W., Fox, J. L., Galand, M., Johnson, R. E., Moses, J. I., et al. (2008). Cross sections and reaction rates for comparative planetary aeronomy. *Space Science Reviews*, *139*, 63-105. doi: 10.1007/s11214-008-9383-7

Huestis, D. L., Slanger, T. G., Sharpee, B. D., & Fox, J. L. (2010). Chemical origins of the Mars ultraviolet dayglow. *Faraday Discussions*, *147*, 307–322.

Jain, S. K., Bougher, S. W., Deighan, J., Schneider, N. M., Gonzlez Galindo, F., Stewart, A. I. F., et al. (2020). Martian thermospheric warming associated with the Planet Encircling Dust Event of 2018. *Geophysical Research Letters*, *47*(3), e2019GL085302. doi: 10.1029/2019GL085302

Jain, S. K., Soto, S., Evans, J. S., Deighan, J., Schneider, N. M., & Bougher, S. W. (2021). Thermal structure of Mars middle and upper atmospheres: Understanding the impacts of dynamics and of solar forcing. *Icarus*. doi: 10.1016/j.icarus.2021.114703

Jain, S. K., Stewart, A. I. F., Schneider, N. M., Deighan, J., Stiepen, A., Evans, J. S., et al. (2015). The structure and variability of Mars upper atmosphere as seen in MAVEN/IUVS dayglow observations. *Geophys. Res. Lett.*, *42*, 9023-9030. doi: 10.1002/2015GL065419

Kasprzak, W. T., Keating, G. M., Hsu, N. C., Stewart, A. I. F., Coldwell, W. B., & Bougher, S. W. (1997). Solar Cycle Behavior of the Thermosphere, in *Venus II: Geology, Geophysics, Atmosphere and Solar Wind Environment* (S. W. Bougher, D. Hunten, & R. J. Phillips, Eds.). University of Arizona: University of Arizona Press.

Keating, G. M., Bougher, S. W., Theriot, M. E., & Tolson, R. H. (2008). Properties of the Mars upper atmosphere derived from accelerometer measurements. In *Proceedings of the 37th cospar scientific assembly.* (Montreal, Canada)

Keating, G. M., Theriot, M. E., Tolson, R. H., Bougher, S. W., Forget, F., i Coll, M. A., & Forbes, J. M. (2003). Recent detection of winter polar warming in the Mars upper atmosphere. In *The third international mars polar science*

–38–

878   *conference* (p. 8033). (Pasadena, California)

879   Krasnopolsky, V. A. (2010). Solar activity variations of thermospheric temperatures

880   on Mars and a problem of CO in the lower atmosphere. *Icarus*, *207*, 638–647.

881   doi: 10.1016/j.icarus.2009.12.036

882   Leblanc, F., Chaufray, J. Y., Lilensten, J., Witasse, O., & Bertaux, J.-L.   (2006).

883   Martian dayglow as seen by the SPICAM UV spectrograph on Mars Express.

884   *Journal of Geophysical Research*, *111*(E09S11). doi: 10.1029/2005JE002664

885   Lee, Y., Combi, M. R., Tenishev, V., Bougher, S. W., & Lillis, R. J.   (2015).   Hot

886   oxygen corona at Mars and the photochemical escape of oxygen: Improved

887   description of the thermosphere, ionosphere and exosphere.   *J. Geophys. Res.*

888   *Planets*, *120*, 1880-1892. doi: 10.1002/2015JE004890

889   Machol, J., Snow, M., Woodraska, D., Woods, T., Viereck, R., & Coddington, O.

890   (2019).   An improved Lyman-alpha composite.   *Earth and Space Science*, *6*

891   *(12)*, 2263-2272. doi: 10.1029/2019EA000648

892   Mahaffy, P. R., Benna, M., Elrod, M., Yelle, R. V., Bougher, S. W., Stone, S. W., et

893   al. (2015). Structure and composition of the neutral upper atmosphere of Mars

894   from the MAVEN NGIMS investigation.   *Geophys. Res. Lett.*, *42*, 8951-8957.

895   doi: 10.1002/2015GL065329

896   Medvedev, A. S., González-Galindo, F., Yiğit, E., Feofilov, A. G., Forget, F., & Har-

897   togh, P.   (2015).   Cooling of the Martian thermosphere by CO_2 radiation and

898   gravity waves: An intercomparison study with two general circulation models.

899   *J. Geophys. Res. Planets*, *120*, 913-927. doi: 10.1002/2015JE004802

900   Nier, A., & McElroy, M. B.   (1977).   Composition and structure of Mars' up-

901   per atmosphere: Results from the Neutral Mass Spectrometers on Viking

902   1 and 2.   *Journal of Geophysical Research*, *82*(28), 4341–4349.   doi:

903   10.1029/JS082i028p04341

904   Pilinski, M., Bougher, S. W., Greer, K., Thiemann, E., Andersson, L., Benna, M.,

905   et al.   (2018).   First evidence of persistent night-time temperature structures

906   in the neutral thermosphere of Mars.   *Geophys. Res. Lett.*, *45*, 8819-8825.   doi:

907   10.1029/2018GL078761

908   Ridley, A., Deng, Y., & Tòth, G.   (2006).   The Global Ionosphere-Thermosphere

909   Model. *J. Atmos. Sol-Terr. Phys.*, *68*, 839. doi: 10.1016/j.jastp.2006.01.008

Roeten, K. J., Bougher, S. W., Benna, M., Elrod, M., Medvedev, A., & Yigit, E. (2022). Impacts of gravity waves in the Martian thermosphere using M-GITM coupled with a whole atmosphere gravity wave scheme. *J. Geophys. Res. Planets*, *Accepted*. doi: 10.1029/2022JE007477

Roeten, K. J., Bougher, S. W., Benna, M., Mahaffy, P. R., Lee, Y., Pawlowski, D., et al. (2019). MAVEN/NGIMS thermospheric neutral wind observations: Interpretation using the M-GITM general circulation model. *Journal of Geophysical Research: Planets*, *124*(12), 3283-3303. doi: 10.1029/2019JE005957

Seiff, A., & Kirk, D. B. (1977). Structure of the atmosphere of Mars in summer at mid-latitudes. *Journal of Geophysical Research*, *82*(28), 4364–4378. doi: 10.1029/JS082i028p04364

Snowden, D., Yelle, R.-V., Cui, J., Wahlund, J.-E., Edberg, N. J. T., & Agren, K. (2013). The thermal structure of Titan's upper atmosphere: 1. Temperature profiles from Cassini INMS observations. *Icarus*, *226*, 552-582. doi: 10.1016/j.icarus.2013.06.006

Stewart, A. I. (1972). Mariner 6 and 7 Ultraviolet Spectrometer experiment: Implications for CO_2+, CO and O airglow. *Journal of Geophysical Research*, *77*, 54-68. doi: 10.1029/JA077i001p00054

Stewart, A. I., Barth, C., Hord, C., & Lane, A. (1972). Mariner 9 Ultraviolet Spectrometer experiment: Structure of Mars' upper atmosphere. *Icarus*, *17*(2), 469–474. doi: 10.1016/0019-1035(72)90012-7

Stewart, A. I. F. (1987). Revised time dependent model of the Martian atmosphere for use in orbit lifetime and sustenance studies. In *LASP-JPL Internal Report, NQ-802429.* (Jet Propulsion Laboratory)

Stone, S. W., Yelle, R. V., Benna, M., Elrod, M., & Mahaffy, P. R. (2018). Thermal structure of the Martian upper atmosphere from MAVEN NGIMS. *J. Geophys. Res. Planets*, *123*, 2842-2867. doi: 10.1029/2018JE005559

Thaller, S. A., Andersson, L., Thiemann, E., Pilinski, M. D., Fang, X., Elrod, M., et al. (2021). Martian nonmigrating atmospheric tides in the thermosphere and ionosphere at solar minimum. *Icarus*. doi: 10.1016/j.icarus.2021.11476

Thiemann, E. M., Eparvier, F. G., Bougher, S. W., Dominique, M., Andersson, L., Girazian, Z., et al. (2018). Mars thermospheric variability revealed by MAVEN/EUV Solar Occultations: Structure at aphelion and perihe-

lion, and response to EUV forcing. *J. Geophys. Res.*, *123*, 2248-2269. doi: 10.1029/2018JE005550

Thiemann, E. M. B., Chamberlin, P. C., Eparvier, F. G., Templeman, B., Woods, T. N., Bougher, S. W., et al. (2017). The MAVEN EUVM model of solar spectral irradiance variability at Mars: Algorithms and results. *Journal of Geophysical Research: Space Physics*, *122*(3), 2748-2767. doi: 10.1002/2016JA023512

Withers, P. (2006). Mars Global Surveyor and Mars Odyssey accelerometer observations of the Martian upper atmosphere during aerobraking. *Geophys. Res. Lett.*, *33*. doi: 10.1029/2005GL024447

Yiğit, E., Aylward, A. D., & Medvedev, A. S. (2008). Parameterization of the effects of vertically propagating gravity waves for thermosphere general circulation models: Sensitivity study. *J. Geophys. Res.*, *113*, D19106. doi: 10.1029/2008JD010135

Zurek, R. W., Tolson, R. A., Bougher, S. W., Lugo, R. A., Baird, D. T., & Bell, o., J. M. (2017). Mars thermosphere as seen in MAVEN Accelerometer data. *Journal of Geophysical Research: Space Physics*, *122*(3), 3798-3814. doi: 10.1002/2016JA023641